



저작자표시-비영리-동일조건변경허락 2.0 대한민국

이용자는 아래의 조건을 따르는 경우에 한하여 자유롭게

- 이 저작물을 복제, 배포, 전송, 전시, 공연 및 방송할 수 있습니다.
- 이차적 저작물을 작성할 수 있습니다.

다음과 같은 조건을 따라야 합니다:



저작자표시. 귀하는 원저작자를 표시하여야 합니다.



비영리. 귀하는 이 저작물을 영리 목적으로 이용할 수 없습니다.



동일조건변경허락. 귀하가 이 저작물을 개작, 변형 또는 가공했을 경우에는, 이 저작물과 동일한 이용허락조건하에서만 배포할 수 있습니다.

- 귀하는, 이 저작물의 재이용이나 배포의 경우, 이 저작물에 적용된 이용허락조건을 명확하게 나타내어야 합니다.
- 저작권자로부터 별도의 허가를 받으면 이러한 조건들은 적용되지 않습니다.

저작권법에 따른 이용자의 권리는 위의 내용에 의하여 영향을 받지 않습니다.

이것은 [이용허락규약\(Legal Code\)](#)을 이해하기 쉽게 요약한 것입니다.

[Disclaimer](#)

공학박사 학위논문

**Large-Area Assembly and
Restructuring of Multiscale
Multidimensional Nanoparticle
Structures and Their Application
to a Solar Cell**

멀티스케일 다차원 나노입자 구조물 대면적
조립 및 재구조화 이의 태양전지 응용

2015 년 2 월

서울대학교 대학원

기계항공공학부

하 경 연

Large-Area Assembly and Restructuring of Multiscale Multidimensional Nanoparticle Structures and Their Application to a Solar Cell

Kyungyeon Ha

School of Mechanical and Aerospace Engineering

The Graduate School

Seoul National University

Abstract

In order to utilize unique and superior properties of nanomaterials in various fields including modern sciences and engineering, many researches for developing nanomaterials have been reported. In particular, multifunctional properties of multiscale multidimensional structures have attracted great interests for numerous applications such as photonics, sensors, and electronics. Therefore, fabrication methods of multiscale multidimensional structures have been continuously studied. As part of the effort, ion assisted aerosol lithography (IAAL) was introduced as a new technique for multiscale multidimensional assembly of nanoparticles. However, to extend applicability of multiscale multidimensional nanoparticle structures (NPSs) via IAAL showing superior properties, researches for large-area patterning and stiffness increase of NPSs are

required. With this motivation, in this study, fundamental techniques to develop IAAL were suggested, and their feasibility was verified by realizing a new-concept nanodevice.

A new technique for large-area assembly of multiscale multidimensional NPSs was proposed by combining IAAL and a multi-spark discharge method. And, three-dimensional (3D) NPSs were uniformly constructed via IAAL utilizing a newly designed multi-pin spark discharge generator over a large area of 50 mm x 50 mm in a parallel manner. The effect of particle sizes on morphologies of NPSs was also studied. In addition, we produced 3D back reflectors based on various 3D NPSs showing superior performance relative to back reflectors fabricated by conventional fabrication methods.

A study on stiffness increase of NPSs via an electron-beam (e-beam) sintering method was performed as another effort to broaden applicability of multiscale multidimensional NPSs. We defined principle of e-beam sintering, and investigated variations in physical properties of NPSs via the e-beam sintering process. Furthermore, a newly combined approach of IAAL and the e-beam sintering technique was developed to fabricate NPSs with unique morphologies.

Based on those fundamental techniques developed herein, we demonstrated a thin-film silicon (Si) solar cell incorporating 3D NPSs with an objective to maximize the light trapping effect. The excellent performance of the thin-film Si solar cell employing 3D NPSs was validated by an experimental comparison with a cell incorporating

nanoparticle clusters and by a theoretical comparison with a cell employing nanobump arrays. And, the thin-film Si solar cell with the 3D NPSs showed a 30% increase in short-circuit current density and a 20% increase in efficiency relative to a flat cell.

Keywords: nanoparticle; assembly; spark discharge; large-area fabrication; electron beam; sintering; photovoltaics; light trapping; 3D structure.

Student Number: 2009-20737

Contents

Abstract	i
Contents	iv
List of Tables	vi
List of Figures	vii
Nomenclature	xiii
Chapter 1. Introduction	1
1.1. Background of Research	2
1.2. Objectives for Research	4
Chapter 2. Large-Area Uniform Fabrication Method of Multiscale Multidimensional Nanoparticle Structures	5
2.1. Introduction	6
2.2. Background of Research	9
2.2.1. IAAL for 3D Assembly of Nanoparticles	9
2.2.2. Spark Discharge Method for Generation of Charged Nanoparticles	11
2.3. Experimental Details	14
2.4. Results and Discussion	19
2.4.1. Uniformity of NPSs via IAAL with a Single-Pin SDG	19
2.4.2. Uniformity of NPSs via IAAL with a Multi-Pin SDG	21
2.4.3. Application: 3D back Reflectors	29
2.5. Conclusion	33

Chapter 3. Electron-Beam Sintering Method of Nanoparticle Structures and its application.....	34
3.1. Introduction.....	35
3.2. Background Knowledge for Research	37
3.2.1. Operating Principles of E-Beam Irradiation System.....	37
3.2.2. Sintering by Joule’s Heating	41
3.3. Results and Discussion	44
3.4. Conclusion	58
Chapter 4. Thin-Film Si Solar Cell incorporating 3D Nanoparticle Structures.....	59
4.1. Introduction.....	60
4.2. Experimental Procedure and Simulation.....	62
4.2.1. Fabrication Process for thin-film nc-Si:H solar cells Employing 3D NPS arrays.....	62
4.2.2. Setup for FDTD simulations	66
4.3. Results and Discussion	68
4.3.1. Optical Properties of the 3D BR	68
4.3.2. Optical and Electrical Performance of the 3D Solar Cell .	74
4.3.3. Analysis of Enhanced Factors of the 3D Solar Cell.....	77
4.4. Conclusion	87
Chapter 5. Concluding Remarks	88
References	92
국문초록	108

List of Tables

Table2.1	The actual images of the sample and the SEM images of the NPSs at the location of the pin represented by the red arrow in figure 2.10.
Table2.2	The actual images of the sample and the SEM images of the NPSs at the positions represented by the red and blue arrows in figure 2.11.
Table3.1	E-beam irradiation conditions for the optical measurement of the 3D NPSs.
Table4.1	Top and tilted views of the 3D BR measured by SEM (left) and AFM (middle). Simulation model (right) of the 3D BR using CATIA.
Table4.2	Top, tilted, and cross-sectional views of the 3D solar cell measured by SEM (left) and AFM (middle). Simulation model (right) of the 3D solar cell using CATIA.
Table4.3	Summary of all electrical outcomes of the thin-film nc-Si:H solar cells fabricated in this study. Device architectures are: substrate: nothing or nanostructures (NPCs or 3D NPSs): Ag (300 nm): ZnO:Al (130 nm): nc-Si:H with a 500-nm-thick i-layer: ITO (80 nm).

List of Figures

- Figure 2.1 Scheme for a 3D assembly of nanoparticles through the IAAL technique: the red, yellow, and green arrows represent the growing direction of 3D NPSs, the direction of coming charged nanoparticles, and the repelling electric fields, respectively.
- Figure 2.2 Two different configurations of SDG. (a) Pin-to-plate type electrode configuration. (b) Rod-to-rod type electrode configuration. Ag nanoparticles generated by spark discharge with a gap distance of 2.5 mm, argon gas flow rate of 3.5 lpm and applied positive potential of 5kV. (c) Size distributions of Ag particles. (d) A TEM image of Ag particles for pin-to-plate type SDG. (e) A TEM image of Ag particles for rod-to-rod type SDG.
- Figure 2.3 Schematics of (a) IAAL with a single-pin SDG, and (b) IAAL with a multi-pin SDG. Both experimental set-ups consist of a spark discharge chamber, a deposition chamber, a corona discharge chamber, and peripheral circuitry.
- Figure 2.4 Actual photos of IAAL set-ups based on (a) a single-pin SDG and (b) a multi-pin SDG.
- Figure 2.5 Enlarged actual images of the spark discharge chamber of (a) the single-pin SDG and (b) the multi-pin SDG. The right image of figure (b) shows the moment when the multiple spark discharges are generated.
- Figure 2.6 Experimental set-up for a particle measurement system.
- Figure 2.7 Variations of height (black-colored closed squares) and diameter (red-colored open squares) of 3D NPSs fabricated by IAAL with a single-pin SDG. The SEM images of 3D NPSs in the inset are shown next to each other to represent the dimensional variations, and the inset photograph shows an

actual image of the sample. The schematic inset illustrates the PR pattern with a 2 μm opening and a 1 μm thickness. Cu nanoparticles were used to construct 3D NPS.

Figure 2.8 (a) Size distributions measured by an SMPS system showing the decrease in the average diameter of the nanoparticles as the flow rate increases from 1, 2, to 3 lpm per hole. Here, d_p , d_g , and σ_g in the inset table represent nanoparticle diameter, geometric mean diameter, and geometric standard deviation, respectively. (b) TEM images showing less agglomeration of generated nanoparticles with an increasing flow rate. The scale bar is 50 nm in length. (c) SEM images of 3D NPSs fabricated via IAAL with the multi-pin SDG revealing the shape variation depending on the generated nanoparticles. The scale bar is 200 nm in length.

Figure 2.9 (a) Distributions of height and diameter of 3D NPSs constructed by IAAL with the multi-pin SDG on each position of the sample. Here, black-colored closed squares and red-colored open squares represent the heights and the diameters, respectively, showing improved uniformity above 95%. The SEM images of 3D NPSs in the inset show the dimensional variations at different positions, and the inset photograph shows an actual sample image fabricated within a size of 50 mm \times 50 mm. (b) An SEM image revealing the part of the 3D NPS array fabricated on a Si-substrate, where the inset shows the 3D NPS formed inside each hole. The scale bar is 10 μm .

Figure 2.10 The effect of the distance between the ground electrode and the sample on the uniformity of 3D NPSs fabricated by IAAL with the multi-pin SDG.

Figure 2.11 The effect of the number of pins on the uniformity of 3D NPSs fabricated by IAAL with the multi-pin SDG.

Figure 2.12 SEM images of 3D NPS arrays fabricated via IAAL with the multi-pin SDG by increasing the deposition time (a)–(c),

where the cross SiO₂ patterns and Ag nanoparticles were used. The inset in each SEM image shows 3D NPSs formed inside each cross SiO₂ pattern with the denoted dimensions. All scale bars are 2 μm in length.

Figure 2.13 SEM images of Ag coated 3D NPS samples created by depositing 300 nm-thickness Ag film on the 3D NPS arrays through the sputtering process. (a) Pre-patterned SiO₂/Si, (b) cross bump-shaped, (c) pyramid-shaped, and (d) bud-shaped 3D NPS samples coated with Ag film. All scale bars are 1 μm in length. (e) Diffuse reflectance and (f) total reflectance of the samples were measured by using a UV-Vis-NIR spectrophotometer in a spectral range of 300 to 1100 nm.

Figure 3.1 Schematic illustration of the inner structure of the SEM column.

Figure 3.2 The distributions of the e-beam within the specimen depending on the acceleration voltage and the specimen type.

Figure 3.3 Schematic illustration of a model for the calculation of Joule's heating at the particle-particle and particle-surface interfaces.

Figure 3.4 The Change in the surface morphology of the NPS as time passes. The scale bar is 100 nm in length.

Figure 3.5 The Change in the surface morphology of the NPS as time passes. The scale bar is 100 nm in length.

Figure 3.6 The variation in the porosity of the NPS via the e-beam irradiation: (a) before and (b) after e-beam treatment. All scale bars are 200 nm in length.

Figure 3.7 Rigidity test of the 3D NPSs sintered by the e-beam. (a) Fabrication of the 3D NPSs via IAAL. (b) Selective irradiation of the e-beam onto the 3D NPSs using a conductive mask having openings. After the sonication process: (c) the actual image of the sample, (d) the 3D NPSs in the region exposed by the e-beam, and (e) the 3D NPSs in the region where the e-beam wasn't irradiated.

- Figure 3.8 (a) Schematic illustration of the electrical measurement using conductive AFM. The red line represents the current flow. (b) I-V curves with respect to the power of the irradiated e-beam.
- Figure 3.9 The variation in the morphologies of the NPSs through the e-beam irradiation: (a) before and (b) after e-beam treatment.
- Figure 3.10 Selective sintering of the 3D NPS array. The scale bare is 1 μm in length.
- Figure 3.11 Variations in the scattering intensities of the NPSs with increasing the power of the e-beam.
- Figure 3.12 Fabrication of the asymmetric pattern via the selective sintering process using the e-beam.
- Figure 4.1 Schematized process of manufacturing a 3D solar cell (a) 3D NPSs (NPSs) used as a template of the 3D solar cell are uniformly constructed via ion assisted aerosol lithography (IAAL) on a Si substrate. The inset reveals the process of IAAL: the yellow arrow represents the direction of charged nanoparticles migrating along with the distorted equipotential surfaces induced by accumulated positive ions on the surface of the SiO₂ film. (b) Spin-on-glass (SOG) coating process for eliminating the undercuts between the 3D NPSs and the SiO₂ film. The 3D solar cell is produced by depositing (c) Ag, (d) ZnO:Al, nc-Si:H (nip configuration, an intrinsic layer = 500 nm), and ITO films on the 3D NPS array.
- Figure 4.2 SEM images indicating each fabrication process for the 3D solar cell: (a) 3D NPSs fabricated on the Si substrate and the physical dimension of the used SiO₂ pattern in the inset; (b) Ag-coated 3D NPSs called 3D back reflector (BR) in this study; (c) the tilted view of the 3D solar cell. (d) Schematic illustration of the 3D solar cell. (e, f) SEM images of each cross section of the 3D solar cell. All scale bars are 500 nm in length.
- Figure 4.3 Total and diffuse reflectance (TR and DR) curves of the three-

type BRs. Black (squares), red (dots), and blue (triangles) lines represent the flat, nanoparticle clusters (NPCs), and 3D BRs, respectively.

Figure 4.4 (a) Schematic illustrations of the 3D BR fabricated by three steps (fabrication of the 3D NPSs via IAAL, spin-on glass (SOG) process on the 3D NPSs, and deposition of a 300-nm-thick Ag film on the 3D NPSs). (b) SEM and (c) the dark-field (DF) images of the 3D BR (scale bar: 1 μm).

Figure 4.5 (a) Simulation model of the 3D BR. Profiles of the electric field intensities of the 3D BR at representative resonance wavelengths (λ_1 - λ_3) in the DR curve of the figure 4.3 with respect to the z axis: (b) z=150 nm, (c) z=310 nm, (d) z=350 nm.

Figure 4.6 SEM images show top views of (a) the 3D NPSs and (b) the NPCs. (scale bar: 2 μm)

Figure 4.7 (a) Current density-voltage (J-V) curves and (b) external quantum efficiencies (EQEs) of the champion flat (squares), NPC (dots), and 3D (triangles) solar cells, absorption curves of the three cells in the inset of figure 4.7 (b).

Figure 4.8 The simulated model for calculating the effect of (a) the 3D BR surrounded by the ZnO:Al/nc-Si:H layers. Calculated results of (b) scattering intensities of the flat (black line) and 3D (red line) BRs.

Figure 4.9 The simulated model for calculating the effect of (a) the 3D front contact. (b) Transmittance enhancement in nc-Si:H (blue line) induced only by the 3D front contact.

Figure 4.10 (a) Schematic illustration of the 3D solar cell for calculating the generation rate in the nc-Si:H layer. (b) Cross sections of each optical generation rate in nc-Si:H at the four wavelengths (λ_1 - λ_4 in figure 4.8 (b)) indicating the representative resonance locations of the 3D BR.

Figure 4.11 Schematic illustration of the cross section of the calculated

cell design. The right part of the image shows the detail information of the physical dimensions of the 3D BR.

Figure 4.12 Schematic illustration of the cross section of the calculated devices employing diverse nanostructured BRs: (a) 3D BR; regularly ordered nanobumps (NBs) with the (b) minimum (NBA_{\min}) and (c) maximum (NBA_{\max}) dimensions of the 3D BR as their diameters.

Figure 4.13 Simulated absorption of various thin-film nc-Si:H solar cells. Black and red lines represent the flat and 3D solar cells, respectively. Green and blue lines represent cells employing NBA_{\min} and NBA_{\max} , respectively.

Figure 4.14 Power absorbed in the nc-Si:H layer of the calculated devices. Black and red lines represent the flat and 3D solar cells, respectively. Green and blue lines represent solar cells employing NBA_{\min} and NBA_{\max} , respectively.

Figure 4.15 (a) Schematic illustration indicating various locations of cross-section views of the 3D solar cell. (b) The cross-section views of the optical generation rates in the nc-Si:H layers of the 3D, NBA_{\min} , and NBA_{\max} solar cells at the various locations (A-A', B-B', C-C', and D-D').

Nomenclature

d_g	Geometric mean diameter
σ_g	Geometric standard deviation
T	Particle temperature
Q	Joule's heating
v	Particle volume
$c_{v,p}$	Specific heat capacity
I_p	Current passing through nanoparticles
R_c	Contact resistance at particle-particle and particle-surface interfaces
t	Time period
ρ_c	Resistivity of the material at contact
z_0	Distance between nanoparticle
A_c	Contact area
r	Nanoparticle diameter
a	Contact radius
λ	Wavelength
ε''	Imaginary part of permittivity
E	Electric field
h	Dirac constant

Chapter 1.

Introduction

1.1. Background of Research

In recent years, multiple functions (Lakes et al., 1993; Ko et al., 2008; Yusko et al., 2011) resulting from multiscale multidimensional structures have received great attention in diverse fields such as electronics (Ye et al., 2004; Tseng et al., 2007), optics (Henzie et al., 2007; Wurtz et al., 2011), chemistry (Srivastava et al., 2006), and biomimetics (Choi et al., 2009). Therefore, various fabrication methods for multiscale multidimensional structures (Nie et al., 2008; Carlson et al., 2012; Bae et al., 2014) have been constantly developed worldwide.

Although serial approaches such as electron-beam (e-beam) lithography (Cho et al., 2009), ion-beam lithography (Fudouzi et al., 2002), and atomic force microscopy lithography (Lyuksyutov et al., 2003) have made enormous progress in nanoscience, there still remains challenges in overcoming throughput constraints and in enabling large-area fabrication for their practical use. Aside from the serial methods, a variety of parallel approaches such as interferometric lithography (Xia et al., 2011) and block copolymer self-assembly (Ross et al., 2014) have been proposed. While various structures can be fabricated through those parallel methods, there are still limitations of pattern diversity with respect to the scale and dimensional aspects.

Our research group has discovered a new methodology for multiscale multidimensional assembly of nanoparticles, which is named ion assisted aerosol lithography (IAAL) (Kim et al., 2006; Lee et al., 2009; Lee et al.,

2010; You et al., 2010; Woo et al., 2011; Kim et al., 2011; Jung et al., 2014). As one of the parallel fabrication methods, it features the capability with nanoscale accuracy and high reproducibility for multiscale multidimensional structuring and positioning of nanoparticles on the desired location. However, large-area fabrication and improved mechanical durability of nanoparticle structures (NPSs) are essential prerequisites for industrialization of this nanoparticle assembly technique.

With this motivation, we suggested a new route combining IAAL and a multi-spark discharge method (Ha et al, 2014; Han et al., 2012) for wafer-scale patterning of the multiscale multidimensional NPSs with ensuring uniformity. We also discovered a facile method to enhance the mechanical durability of NPSs utilizing e-beam. These fundamental techniques widen applicability of multifunctional properties of multiscale multidimensional NPSs in various fields.

1.2. Objectives for Research

The main purpose of this research is to develop fundamental techniques to extend the applicability of multiscale multidimensional NPSs constructed by IAAL, and to show the feasibility of those techniques by manufacturing a thin-film Si solar cell employing three-dimensional (3D) NPSs. As previously demonstrated in many researches (Kim et al., 2006; Lee et al., 2009; Lee et al., 2010; You et al., 2010; Woo et al., 2011; Kim et al., 2011; Jung et al., 2014), any charged aerosols (various materials such as metal, oxide, protein, etc.) can be precisely assembled by IAAL on a desired position with a nanoscale resolution in a parallel manner. Plus, IAAL is cost-effective because the process is carried out under atmospheric pressure. Therefore, this study has a significant meaning in developing the effective IAAL by accomplishing large-area fabrication and stiffness increase of NPSs, which is required to use the multiscale multidimensional NPSs in diverse applications. Thus, in order to fulfill the purpose of this study, three researches were carried out: a large-scale uniform fabrication method of multiscale multidimensional NPSs utilizing a newly designed multi-pin spark discharge generator; the improvement in the rigidity of NPSs through the e-beam sintering process; and fabrication of a thin-film silicon solar cell incorporating three-dimensional (3D) NPSs based on the two fundamental techniques.

Chapter 2.

Large-Area Uniform Fabrication

Method of Multiscale

Multidimensional Nanoparticle

Structures

2.1. Introduction

Combinatorial assembly of building blocks such as nanoparticles (Dong et al., 2011), diblock copolymers (Tavakkoli et al., 2012; Liu et al., 2012), and DNAs (Mirkin et al., 1996; Chi et al., 2012) is one of promising candidates for constructing multidimensional (Mu et al., 2011, Bian et al., 2012, Kwon et al., 2012) and multifunctional (Hwang et al., 2012, Kim et al., 2009, Gao et al., 2009) structures. Since the physical properties of these structures are dependent on the size, morphology, composition, and structuring of the building blocks, various nanofabrication methods for multiscale multidimensional structures have been developed for their use in emerging fields such as photonics (Freyman et al., 2010, Zhang et al., 2011, Ergin et al., 2010), sensors (Ponzoni et al., 2006), and catalyst supports (Polshettiwar et al., 2009, Tian et al., 2011). Therefore, precisely controlled synthesis and assembly techniques of the building blocks are required for constructing structures having desired properties.

For nanoparticle synthesis, the spark discharge method (Meuller et al., 2012; Tabrizi et al., 2009; Schwyn et al., 1988) is considered one of the most facile and reliable methods generating high-purity nanoparticles with thermal stability, high crystallinity, and a narrow size distribution among gas phase routes (Swihart et al., 2003, Kruis et al., 1998). The particle diameter can be easily controlled by adjusting diverse parameters including spark energy, flow rate of carrier gas (Meuller et al., 2012, Tabrizi et al., 2009), and geometries (Han et al., 2012). In addition, homogeneous and

binary nanoparticles (Tabrizi et al., 2009, Byeon et al., 2008) can be produced utilizing single and dual conductive materials as electrodes, respectively.

Apart from the progress on nanoparticle synthesis, many researches have been introduced for the assembly of nanoparticles using various fundamental external forces (Min et al., 2008), such as electrostatic (Fudouzi et al., 2002, Krinke et al., 2001, Kim et al., 2006, Krinke et al., 2002, Prost et al., 1998), magnetic (Wolf et al., 2005, Demirors et al., 2013), and capillary forces (Kraus et al., 2007, Lin et al., 2003). Among these, ion assisted aerosol lithography (IAAL) has the capability to construct multiscale multidimensional nanoparticle structures (NPSs) with nanoscale resolution at room temperature and atmospheric pressure in a parallel fashion (Kim et al., 2006; Lee et al., 2009; Lee et al., 2010; You et al., 2010; Woo et al., 2011; Kim et al., 2011; Jung et al., 2014). In spite of these superior features of IAAL, wafer-scale fabrication with reliable uniformity remains a challenge for its practical use in industrial applications.

With this motivation, we proposed a new large-scale uniform fabrication method of multiscale multidimensional NPSs via a combined approach of IAAL and multi-spark discharge. The size distributions and the morphologies of the nanoparticles generated by a newly designed multi-pin spark discharge generator (SDG) were studied with respect to flow rates of carrier gas, and the particle size effect on the morphologies of three-dimensional (3D) NPSs was investigated. Then, the uniformities

of 3D NPSs formed by the multi-pin SDG was examined and compared with those of a conventional single-pin case, and the parameter studies on the uniformities were conducted. Lastly, new-concept 3D back reflectors with superior performance were realized to show the feasibility of the large-area patterning technique.

2.2. Background of Research

2.2.1. IAAL for 3D Assembly of Nanoparticles

IAAL (Kim et al., 2006; Lee et al., 2009; Lee et al., 2010; You et al., 2010; Woo et al., 2011; Kim et al., 2011; Jung et al., 2014) is a facile way for multiscale multidimensional assembly of nanoparticles. Figure 2.1 shows the schematic illustration of the principle of IAAL. When a negative voltage is applied to a Si substrate with a pre-patterned photoresist (PR), both positively charged nanoparticles and positive ions move toward the substrate. Since ions have much larger electrical mobility than charged nanoparticles, the positive ions earlier arrive at the Si substrate and are accumulated on the PR surface, which creates a lensing effect resulting from the distorted equipotential surfaces as described in the first image of figure 2.1. Plus, the ions on the PR also repel the following charged nanoparticles. Therefore, the nanoparticles are convergently deposited within the exposed regions of the Si substrate in a parallel manner. When we keep depositing the nanoparticles, if the height of the NPSs is shorter than the PR thickness, the NPSs grow only in the vertical direction as depicted in the second image of figure 2.1. However, if the height of the NPSs becomes higher than the PR thickness, the NPSs also start to grow in the lateral direction because of the antenna effect of the neighboring NPSs as seen in the third image of figure 2.1. Various 3D NPSs can be produced by changing experimental parameters such as deposition time, shape of a PR pattern, and particle sizes, which will be explained in section 2.4.

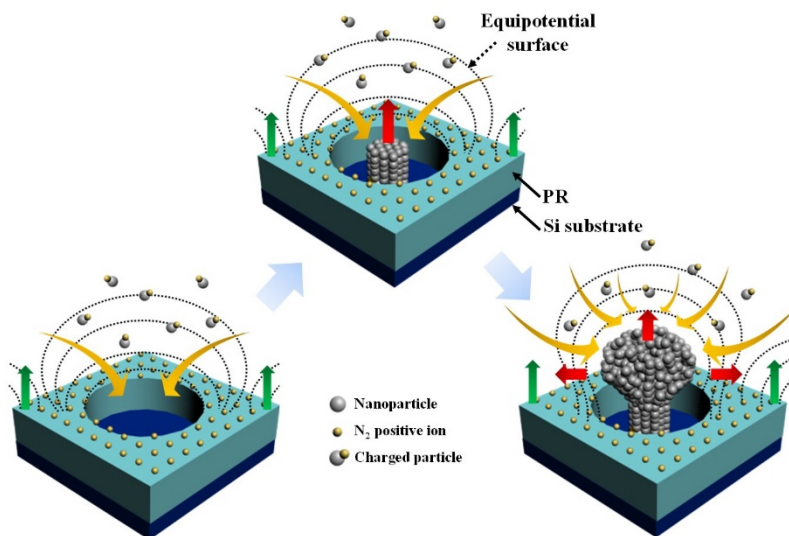


Figure 2.1. Scheme for a 3D assembly of nanoparticles through the IAAL technique: the red, yellow, and green arrows represent the growing direction of 3D NPSs, the direction of coming charged nanoparticles, and the repelling electric fields, respectively (adapted from Ha et al., 2014).

2.2.2. Spark Discharge Method for Generation of Charged Nanoparticles

Among gas phase synthesis (Kruis et al., 1998), spark discharge (Tabrizi et al., 2009) is one of the fascinating method for generation of high-purity nanoparticles. However, there are difficulties in generating unagglomerated nanoparticles utilizing a conventional SDG with a rod-to-rod configuration. For that reason, a new-concept SDG with a pin-to-plate configuration was proposed for generation of unagglomerated and ultrafine nanoparticles (Han et al., 2012) which are required for fabricating stable 3D NPSs. Schematics of the two SDGs are shown in figure 2.2 (a) and (b). The pin-to-plate type SDG has asymmetric electrodes consisting of a pin with a sharp tip as a positive electrode and a grounded plate having a narrow exit hole at the center. When a voltage between the two electrodes becomes higher than a critical point (maximum voltage in corona discharge), spark occurs and increases the temperature of the two electrodes, which results in evaporation of the two electrodes. Then, the evaporated material is rapidly cooled by the carrier gas and becomes nanoparticles. Lastly, the charged nanoparticles are generated by the attachment of the ionized carrier gas. For the pin-to-plate type SDG, since the nanoparticles generated near the exit hole of the plate electrode are immediately transported by the carrier gas, much smaller unagglomerated nanoparticles are produced in comparison to the rod-to-rod type SDG. Figure 2.2 (c), (d), and (e) show the size distributions and the transmission electron microscope (TEM) images of Ag nanoparticles generated by the

pin-to-plate and rod-to-rod SDGs. The gap between the pin and the plate electrodes was fixed at 2.5 mm, and argon gas with flow rate of 3.5 lpm and applied positive potential of 5kV were utilized for the two cases. The geometric mean diameter (d_g) and the geometric standard deviation (σ_g) of Ag nanoparticles generated with the rod-to-rod SDG are about 7.19 nm and 1.59, respectively. On the other hand, the pin-to-plate type SDG produces much smaller unglomerated Ag nanoparticles with a narrow size distribution ($d_g = 5.36$ nm, $\sigma_g = 1.37$) relative to the rod-to-rod case.

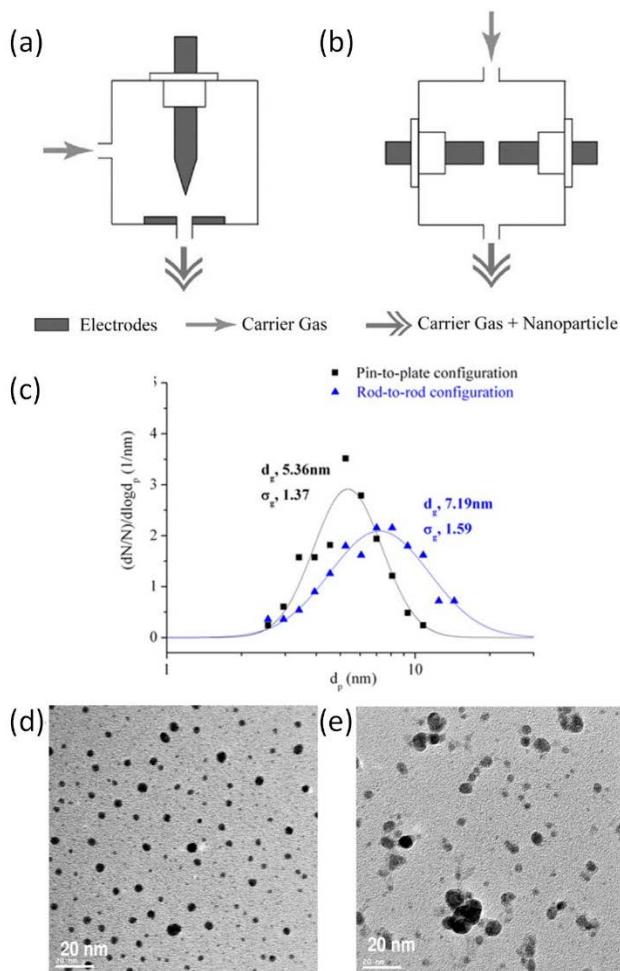


Figure 2.2. Two different configurations of SDG. (a) Pin-to-plate type electrode configuration. (b) Rod-to-rod type electrode configuration. Ag nanoparticles generated by spark discharge with a gap distance of 2.5 mm, argon gas flow rate of 3.5 lpm and applied positive potential of 5kV. (c) Size distributions of Ag particles. (d) A TEM image of Ag particles for pin-to-plate type SDG. (e) A TEM image of Ag particles for rod-to-rod type SDG. (adapted from Han et al., 2012)

2.3. Experimental Details

Schematics of the conventional single-pin SDG and the newly proposed multi-pin SDG are illustrated in figure 2.3. And the actual photos of the two SDGs are shown in figure 2.4. Both spark discharge devices consist of three chambers: a spark discharge chamber for the generation of charged nanoparticles and ions; a deposition chamber where a sample is located; a corona discharge chamber for ion generation. For the single-pin SDG, the amount of generated nanoparticles is small due to the single-pin configuration as seen in figure 2.3 (a). And, since the three chambers are connected by the thin pipes, there are some losses of nanoparticles generated by the spark discharge process resulting from the attachment on the inner wall of the pipes during migration of nanoparticles, which induces long deposition time. However, the main reason of non-uniform patterning of NPSs originates from the movement mechanism of nanoparticles. Charged nanoparticles transport not by the diffusion process but along the electrostatic field formed inside the deposition chamber. Therefore, the charged nanoparticles mainly go straight toward a sample located in the deposition chamber. As a result, NPSs are produced only over a small area. (The detailed information on the single-pin SDG was explained well in the previous study. (Han et al., 2012)) To overcome the limitations of the single-pin SDG, we suggested the multi-pin SDG of the pin-to-plate type (Ha et al., 2014) as shown in figure 2.3 (b). The multi-pin configuration was chosen to increase the amount of nanoparticle generation and to

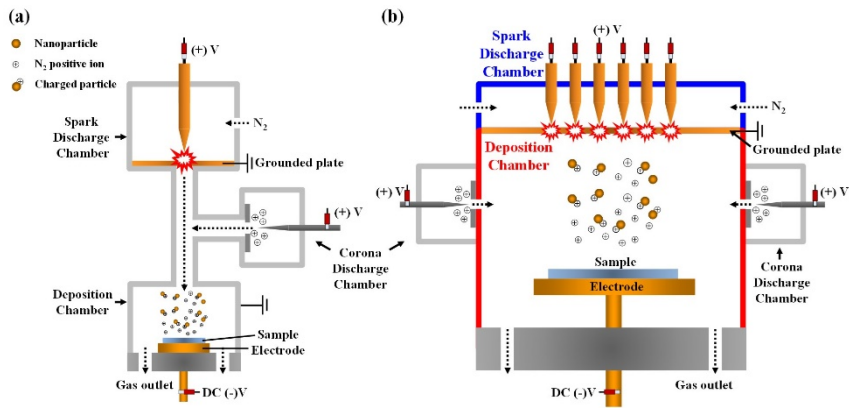


Figure 2.3. Schematics of (a) IAAL with a single-pin SDG, and (b) IAAL with a multi-pin SDG. Both experimental set-ups consist of a spark discharge chamber, a deposition chamber, a corona discharge chamber, and peripheral circuitry (adapted from Ha et al., 2014)

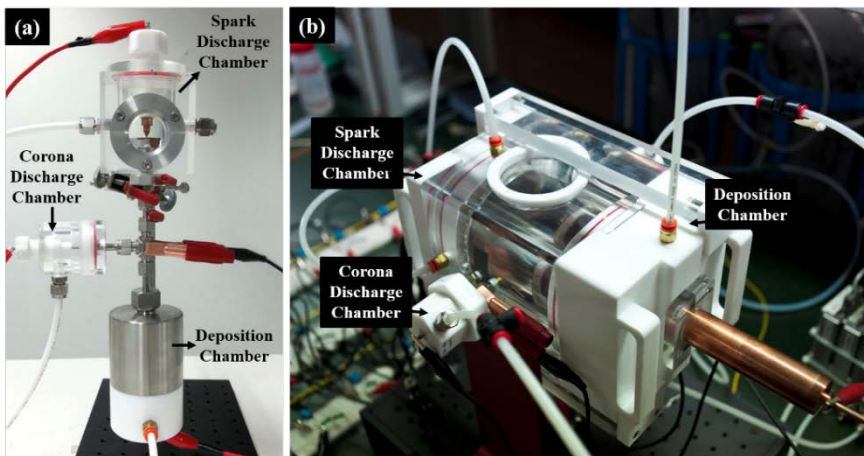


Figure 2.4. Actual photos of IAAL set-ups based on (a) a single-pin SDG and (b) a multi-pin SDG (adapted from Ha et al., 2014).

accomplish the large-scale patterning. Plus, all three chambers were merged as one body for direct deposition of generated nanoparticles, which minimizes the loss of nanoparticles, and thereby the decreased deposition time. The multi-pin spark discharge chamber (the blue color in figure 2.3 (b)) has a volume with an inner diameter of 11.5 cm and a height of 1 cm. Inside the space, 18 pins with a diameter of 4 mm were arrayed with the inter-distance of 18 mm for accomplishing uniform deposition of charged nanoparticles. All pins have a sharp apex with a radius of curvature of approximately 0.13 mm at the end. (see the actual images of the pin electrodes of single-pin and multi-pin SDG in the figure 2.5) A flat plate with 1-mm-diameter exit holes faces the plural pins, and the center of each exit hole coincides with that of each pin electrode within several μm tolerance. The gap between the pin electrode and the plate electrode was fixed at 1 mm, and Ag and Cu were used as representative conductive materials for the electrodes. In this study, the flat plate was utilized as a ground electrode, and a positive high voltage (HV, FuG Elektronik GmbH, HCP 140-12500) applied to each pin electrode through an individually connected electric circuit as shown in figure 2.6. The applied voltage of 4 kV, a resistor (R_c) of 20 M Ω , and a capacitor (C_{ext}) of 2 nF were utilized to produce constant spark energy. The actual image of multiple sparks generated by the multi-pin SDG is shown in figure 2.5 (b). The designed deposition chamber (the red color in figure 2.3) has a volume with an inner diameter of 11.5 cm and a height of 10 cm so that a sample of up to 60 mm \times 60 mm can be loaded. The distance between the grounded flat plate

electrode and the sample was fixed at 7 cm with ensuring uniformity. A negative potential of 4 kV applied to the sample in this study. And, corona discharge chambers were symmetrically placed in the middle side of the deposition chamber for generation of additional positive ions. Nitrogen with a purity of 99.8% was used as carrier gas with the flow rates of 1, 2, and 3 lpm per hole for the multi-pin SDG, while carrier gas with a flow rate of 2 lpm was used for the single-pin case. All experiments using the single-pin SDG were performed under the same conditions of the multi-pin case.

Size distributions of nanoparticles produced by the multi-pin SDG were measured with a scanning mobility particle sizer (SMPS) system composed of an aerosol neutralizer (Kr-85), a differential mobility analyzer (DMA, TSI 3085), and a condensation particle counter (CPC, TSI 3776) as depicted in figure 2.6. Morphologies of the generated nanoparticles was observed by using a high-resolution-transmission electron microscope (HR-TEM, JEOL JEM-2100F). Uniformities and morphologies of 3D NPSs via IAAL using the single-pin and multi-pin SDGs were investigated by a field-emission scanning electron microscope (FE-SEM, Carl Zeiss SUPRA55VP). Optical properties of 3D light back reflectors based on various 3D NPSs were observed by UV-Vis-NIR spectrophotometer (Agilent Technologies, Cary 5000) in a wavelength range from 300 to 1100 nm.

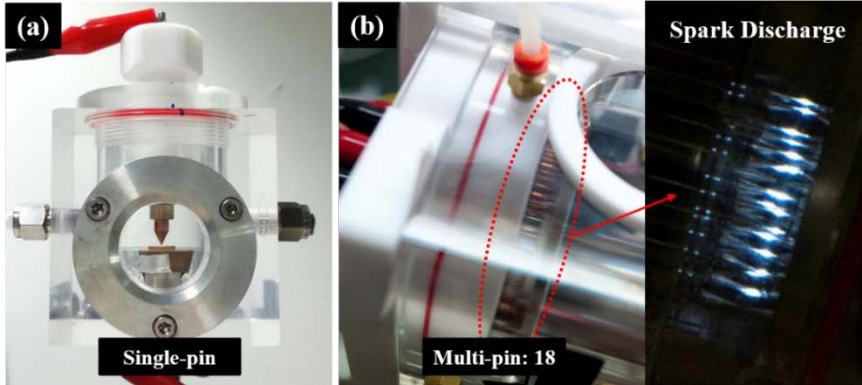


Figure 2.5. Enlarged actual images of the spark discharge chamber of (a) the single-pin SDG and (b) the multi-pin SDG. The right image of figure (b) shows the moment when the multiple spark discharges are generated (adapted from Ha et al., 2014).

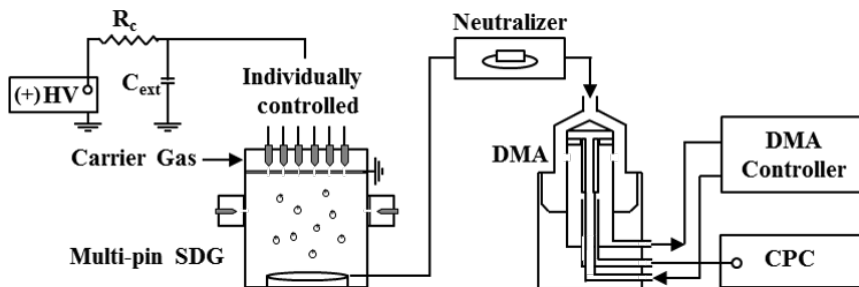


Figure 2.6. Experimental set-up for a particle measurement system (adapted from Ha et al., 2014).

2.4. Results and Discussion

2.4.1. Uniformity of NPSs via IAAL with a Single-Pin SDG

Figure 2.7 indicates the changes in the height and the diameter of Cu NPSs constructed on a Si-substrate of 30 mm× 30 mm via IAAL using the single-pin SDG. The insulating photoresist (PR) film has a pattern with a 2 μm opening (spacing = 4 μm) and a 1 μm thickness as shown in the inset of figure 2.7. Both physical dimensions of the Cu NPSs rapidly decreases with approximately 280 (height) and 40 nm (diameter) per 1 mm distance from the center to the edge of the substrate. Then, nanoparticles were not deposited outside 9 mm from the center. By defining the uniformity [%] as $100 \times (1 - \text{standard deviation}/\text{mean})$, the uniformities of the height and the diameter are estimated to be approximately 7 and 32%, respectively, with mean values of 880 nm (height) and 200 nm (diameter). Here, the ion-induced focusing effect was also validated by the Cu NPSs with the diameter of 200 nm at the 2 mm position showing a ten times reduction in the feature size compared to the PR opening size of 2 μm. This non-uniform growth of the Cu NPSs was caused under the single-pin SDG due to the insufficient time for nanoparticles to spread out over a large area.

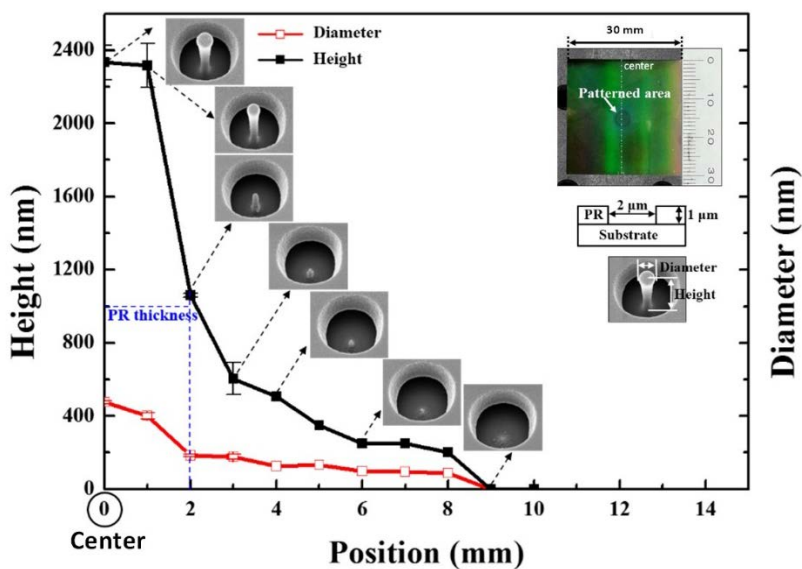


Figure 2.7. Variations of height (black-colored closed squares) and diameter (red-colored open squares) of 3D NPSs fabricated by IAAL with a single-pin SDG. The SEM images of 3D NPSs in the inset are shown next to each other to represent the dimensional variations, and the inset photograph shows an actual image of the sample. The schematic inset illustrates the PR pattern with a 2 μm opening and a 1 μm thickness. Cu nanoparticles were used to construct 3D NPS. (adapted from Ha et al., 2014)

2.4.2. Uniformity of NPSs via IAAL with a Multi-Pin SDG

Firstly, we investigated the size distribution and the morphologies of Cu nanoparticles produced by the multi-pin SDG with respect to the flow rate. As shown in figure 2.8 (a) and (b), the smaller and less agglomerated nanoparticles were generated with increasing the flow rates from 1, 2, to 3 lpm per hole, where the d_g decreased from 5.80, 4.77, to 4.18 nm, respectively, with a reduction in the σ_g . Such trend can be interpreted by the short residence time of the nanoparticles and their low possibility of collision (Meuller et al., 2012, Tabrizi et al., 2009, Han et al., 2012) originating from the faster flow velocity within the deposition chamber with increasing the flow rates. Then, we fabricated the three-type 3D NPSs consisting of the nanoparticles having the different size distributions, and studied the effect of the particle size on the 3D NPSs utilizing the same PR pattern as that of the single-pin case. The three SEM images in figure 2.8 (c) show the obvious difference in the shapes and the porosities of the 3D NPSs with respect to the different-sized nanoparticles. Larger (charged) nanoparticles could not exactly follow the distorted electric field lines caused by the ion-induced lensing effect due to larger inertia, which consequently generates more irregular 3D NPSs in the first image of figure 2.8 (c) (Lee et al., 2010). On the other hand, since it is easier for smaller nanoparticles to follow the electric field lines, more regular and compact 3D NPSs are produced. Therefore, as the smaller nanoparticles generated more with increasing the flow velocity, the denser 3D NPSs were formed as seen in figure 2.8 (c).

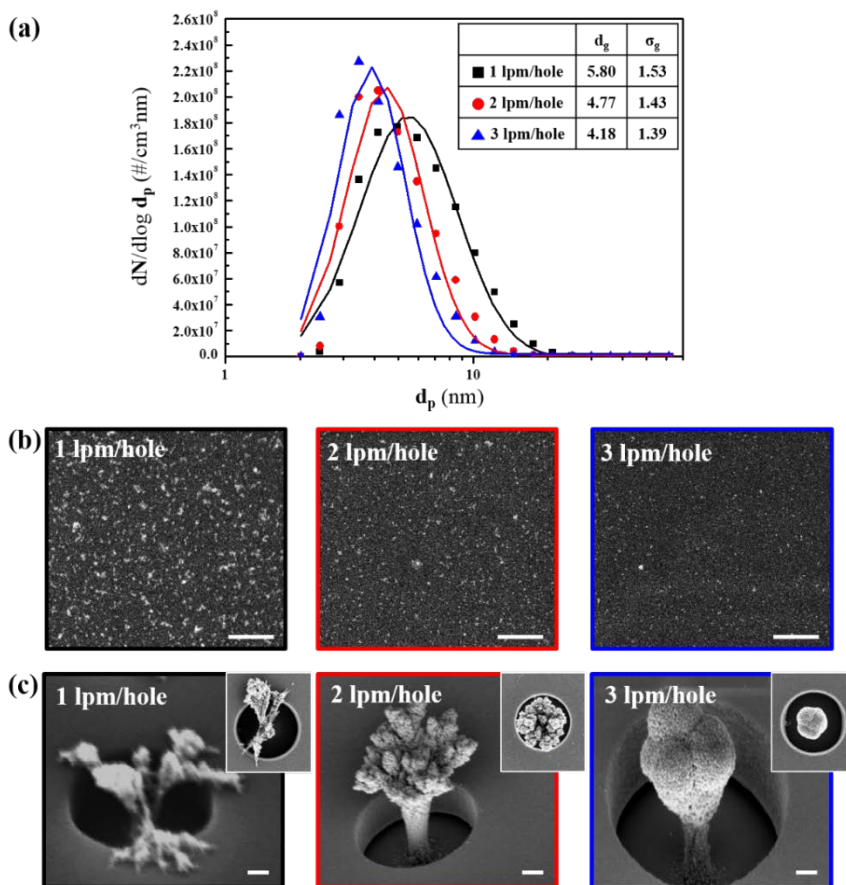


Figure 2.8. (a) Size distributions measured by an SMPS system showing the decrease in the average diameter of the nanoparticles as the flow rate increases from 1, 2, to 3 lpm per hole. Here, d_p , d_g , and σ_g in the inset table represent nanoparticle diameter, geometric mean diameter, and geometric standard deviation, respectively. (b) TEM images showing less agglomeration of generated nanoparticles with an increasing flow rate. The scale bar is 50 nm in length. (c) SEM images of 3D NPSs fabricated via IAAL with the multi-pin SDG revealing the shape variation depending on the generated nanoparticles. The scale bar is 200 nm in length (adapted from Ha et al., 2014).

As a next step, we investigated the uniformity of the physical dimensions of the 3D NPSs via IAAL using the multi-pin SDG. Compact 3D NPSs were constructed on the substrate of 60 mm x 60 mm with the flow rate of 3 lpm per hole. For the efficient fabrication of the 3D NPSs, an insulating mask with a square opening of 53 mm x 53 mm covered a portion of the substrate, which prevents the unnecessary deposition of nanoparticles on the electrode located in the deposition chamber. The distorted equipotential surfaces arising from the ions accumulated on the covered insulating mask induces the nonuniform growth of the 3D NPSs at the edge of the opened area of 53 mm x 53 mm. Consequently, we could uniformly construct the 3D NPSs over a large area of 50 mm x 50 mm. Based on the measured data in figure 2.9 (a), a uniformity of height of approximately 97% is obtained with a mean value of 2000 nm, while the uniformity of diameter is approximately 95% with a mean value of 450 nm, which represents much improved uniformity compared to the single-pin case. The actual image of the sample is shown in the inset of figure 2.9 (a), and the square-shaped and dark-sided region of the sample indicates the patterned area where the 3D NPSs in figure 2.9 (b) were fabricated. Deposition rate of IAAL is dependent on various factors such as particle size, shapes and dimensions of a pre-patterned insulation film, and an exposed region of a substrate. In this experiment, the deposition rate is approximately 0.2 nm s^{-1} with respect to the height of the 3D NPS, which is equivalent to the nanoparticle number deposition rate of $3 \times 10^{10} \text{ s}^{-1}$ in the patterned area, and it can be increased by controlling the experimental

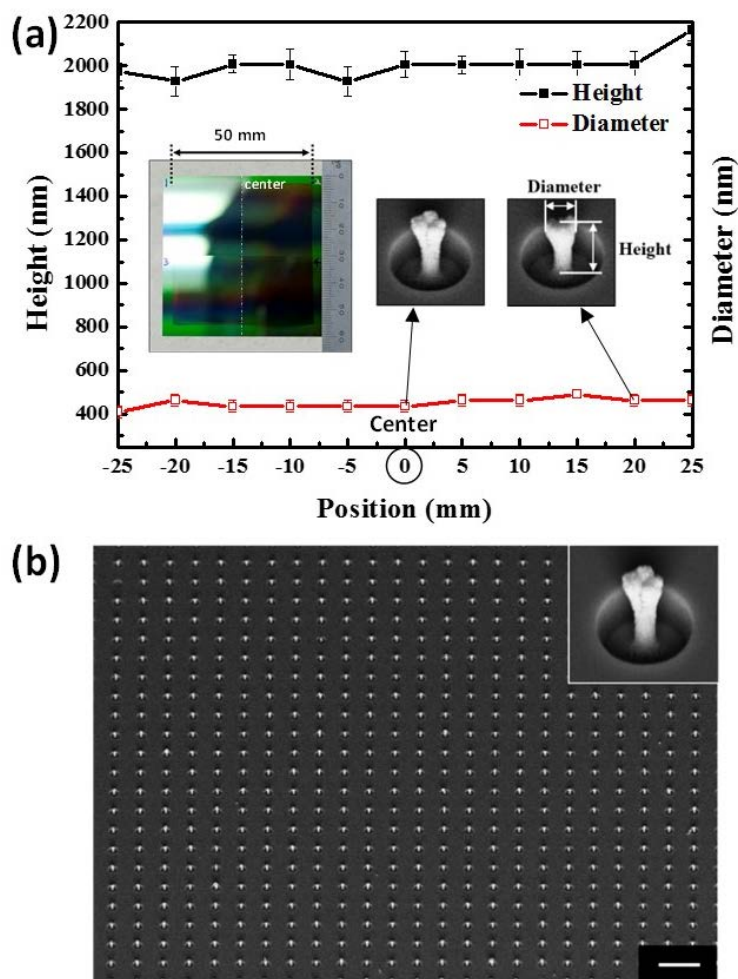


Figure 2.9. (a) Distributions of height and diameter of 3D NPSs constructed by IAAL with the multi-pin SDG on each position of the sample. Here, black-colored closed squares and red-colored open squares represent the heights and the diameters, respectively, showing improved uniformity above 95%. The SEM images of 3D NPSs in the inset show the dimensional variations at different positions, and the inset photograph shows an actual sample image fabricated within a size of 50 mm× 50 mm. (b) An SEM image revealing the part of the 3D NPS array fabricated on a Si-substrate, where the inset shows the 3D NPS formed inside each hole. The scale bar is 10 μ m. (adapted from Ha et al., 2014)

parameters including the number of pins, the electric circuit, the negative voltage applied to the substrate and the distance between the ground electrode and the substrate. Plus, by increasing the number of pins as well as the inner space of the deposition chamber enough, 3D NPSs can be produced in an area larger than 50 mm× 50 mm.

For achieving the large-scale uniform fabrication of 3D NPSs, the number of pins and the distance between the ground electrode and the sample play a critical role. Figure 2.10 shows the effect of the distance between the ground electrode and the sample (called distance hereafter, D) on the uniformity. Here, all experimental conditions were fixed except the distance. As the distance became farther from the ground electrode, the uniformities of the diameter of the 3D NPSs were improved from 54, 84, 90 to 93% with the mean values of 793, 417, 475, and 383 nm, respectively. The increased uniformities were also confirmed by the dark-sided regions in the actual samples in table 2.1. With increasing the distance, the circle-shaped spots representing the locations of the pins faded and eventually disappeared at D = 30 mm, which corresponds well to the measured results in figure 2.10. NPSs with a diameter of 1.2 μm was obtained (PR opening = 2 μm) at D = 10 mm, which means that the ion-induced focusing effect didn't occur as shown in the first SEM image in table 2.1. Due to the strong electric field formed inside the deposition chamber induced by the short distance, the nanoparticles could not follow the distorted electric field lines arising from the accumulated ions on the PR. Further, we found that the distance influences the focusing extent of NPSs. Even with the same PR

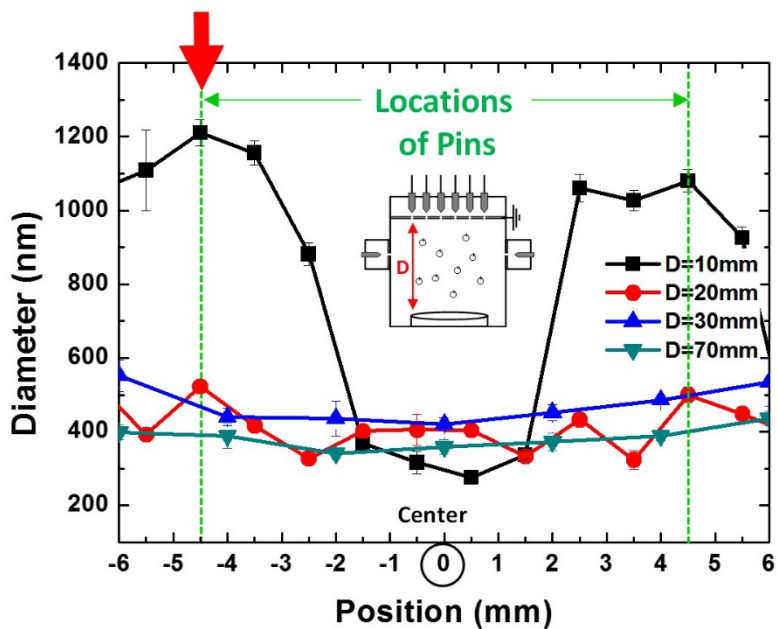


Figure 2.10. The effect of the distance between the ground electrode and the sample on the uniformity of 3D NPs fabricated by IAAL with the multi-pin SDG.

Table 2.1. The actual images of the sample and the SEM images of the NPs at the location of the pin represented by the red arrow in figure 2.10.

D = 10 mm T = 1hr	D = 20 mm T = 1hr	D = 30 mm T = 1hr	D = 70 mm T = 1hr30min

pattern, the NPSs with a diameter of 140 nm were obtained at $D = 30$ mm, whereas the NPSs with a diameter of 400 nm were constructed at $D = 70$ mm (see the SEM images in table 2.1). Such gap is explained by the small amount of ions accumulated on the PR representing the less focusing effect, which results from the weak electric field formed inside the deposition chamber due to the farther distance. Then, we studied the effect of the number of pins on the uniformity of 3D NPSs via IAAL with the multi-pin SDG as seen in figure 2.11. Here, the 3D NPSs were fabricated at $D = 20$ mm, and all experimental conditions were fixed except the number of pins. With increasing the number of pins from 8, 16, to 24, the uniformities of the diameter of the 3D NPSs were improved from 73, 85, to 84% with the mean values of 334, 342, and 417 nm, respectively. The increased uniformities were also confirmed by the actual samples and the SEM images in table 2.2. In addition, we observed the constant uniformity above 16 pins, which demonstrates that 4 pins per unit area [cm^{-2}] are required for the large-area uniform fabrication of 3D NPSs.

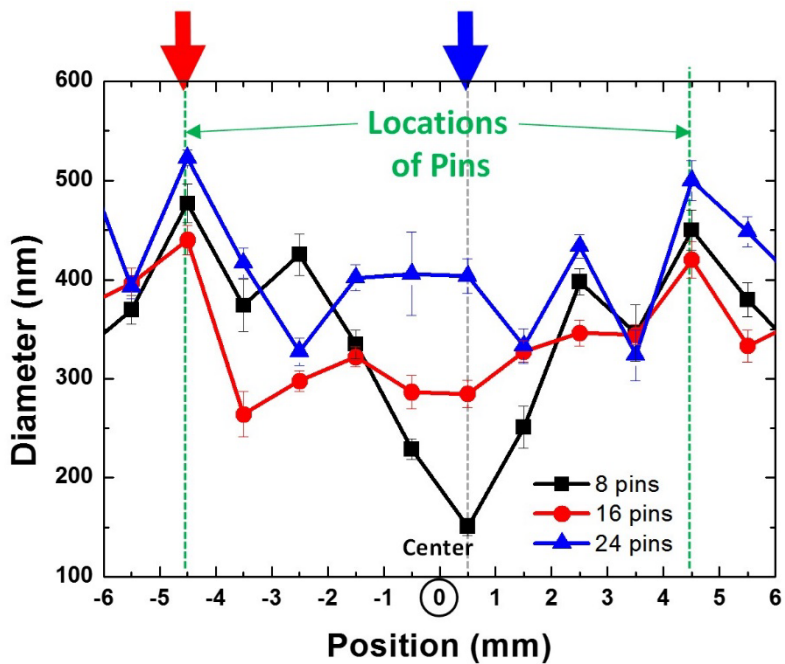


Figure 2.11. The effect of the number of pins on the uniformity of 3D NPSs fabricated by IAAL with the multi-pin SDG.

Table 2.2. The actual images of the sample and the SEM images of the NPSs at the positions represented by the red and blue arrows in figure 2.11.

		Position - 4.5 mm	Position 0.5 mm
8 pins			
24 pins			

2.4.3. Application: 3D back Reflectors

The feasibility of the large-scale patterning method was demonstrated by realizing 3D back reflectors based on various 3D NPSs showing superior performance relative to 1D and 2D back reflectors via conventional fabrication methods. Plus, in order to show the diversity of this technique, 3D NPSs consisting of Ag nanoparticles were produced with an insulating SiO₂ film having a cross-shaped pattern with a 100 nm thickness and a 2 μm period. The detailed dimension of the SiO₂ pattern was described in the inset of figure 2.12 (a). Various shaped 3D NPSs were fabricated with respect to the deposition time of 45, 70, and 200 min as seen in figure 2.12 (a)-(c). By sputtering a 300-nm-thick Ag film on the three 3D NPSs, three-type 3D back reflectors were manufactured. (see figure 2.13 (b)-(d)) Then, we observed the diffuse and total reflectance (DR and TR) of the 3D back reflectors by UV-Vis-NIR spectrophotometer in a wavelength range of 300 to 1100 nm (see figures 2.13 (e) and (f)), and compared the results with a flat Ag film (1D back reflector) and an Ag-coated SiO₂ pattern (2D back reflector, figure 2.13 (a)). From the relation $TR = SR + DR$, the TR of the flat Ag film is only given by the SR since the DR is close to zero as shown in figure 2.13 (e), where the trough of the TR curve at around 325 nm is attributed to the bulk plasma absorption of Ag film (Maier, 2007). For the 3D back reflectors, much enhanced DR, but lowered TR is observed relative to the flat Ag film in figure 2.13 (e) and (f), and the DR of the 3D back reflectors increases with growing the 3D NPSs. Such trend can be interpreted by multiple reflection and trapping of

light via multidimensional and multiscale effects coming from highly curved surfaces and protrusions of the 3D NPSs. In comparison with the Ag-coated SiO₂ pattern, although the 3D back reflector of the cross-bump shape exhibits somewhat poorer DR, the 3D back reflector of the pyramid shape shows the improved DR in the NIR region (approximately 700-900 nm). For the 3D back reflector of the bud shape, the greatest DR was obtained in the multi-spectral range covering UV-Vis-NIR region relative to the Ag-coated SiO₂ pattern and the other two 3D back reflectors. And, the highest DR was observed at around 660 nm, which corresponds the lowest TR. From these results, it was proved that 3D NPSs via IAAL with the multi-pin SDG could be used in photovoltaics and display devices as a new 3D light reflector showing better performance than 1D and 2D back reflectors due to an enhanced diffusive reflectance in a broad spectral range.

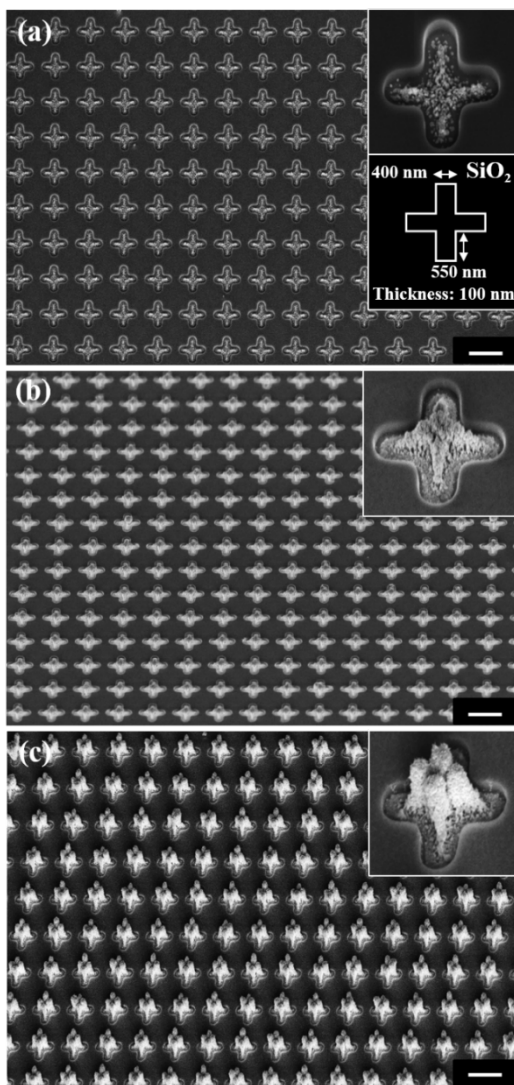


Figure 2.12. SEM images of 3D NPS arrays fabricated via IAAL with the multi-pin SDG by increasing the deposition time (a)–(c), where the cross SiO_2 patterns and Ag nanoparticles were used. The inset in each SEM image shows 3D NPSs formed inside each cross SiO_2 pattern with the denoted dimensions. All scale bars are $2\ \mu\text{m}$ in length (adapted from Ha et al., 2014).

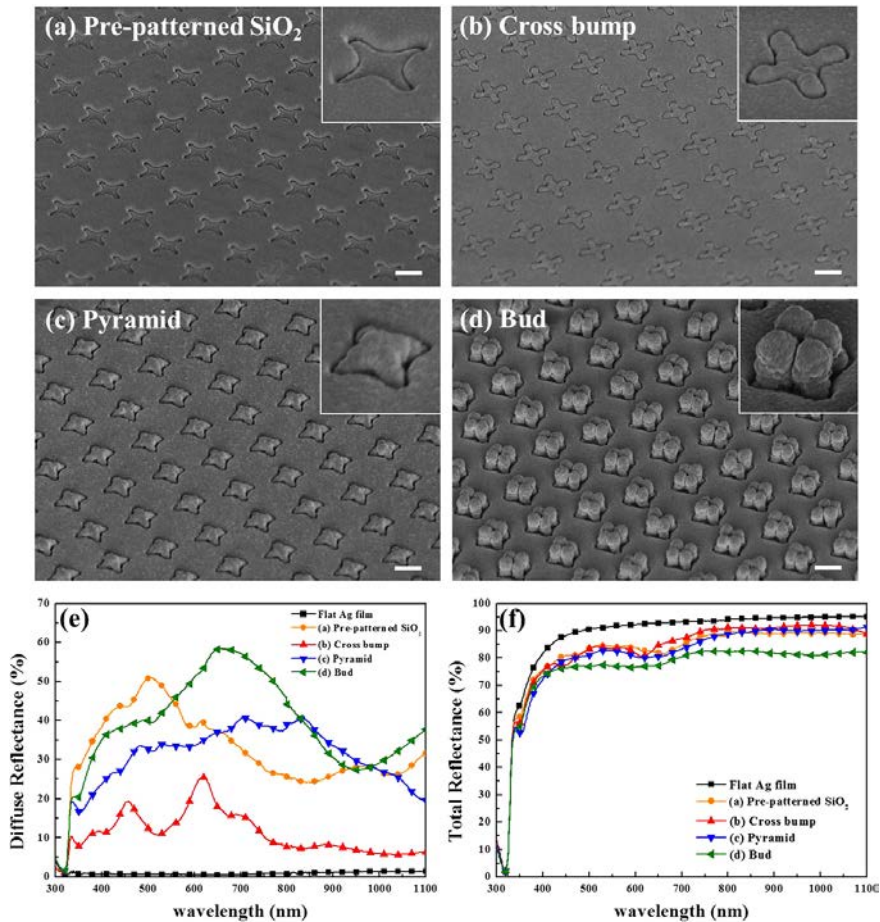


Figure 2.13. SEM images of Ag coated 3D NPS samples created by depositing 300 nm-thickness Ag film on the 3D NPS arrays through the sputtering process. (a) Pre-patterned SiO₂/Si, (b) cross bump-shaped, (c) pyramid-shaped, and (d) bud-shaped 3D NPS samples coated with Ag film. All scale bars are 1 μ m in length. (e) Diffuse reflectance and (f) total reflectance of the samples were measured by using a UV-Vis-NIR spectrophotometer in a spectral range of 300 to 1100 nm. (adapted from Ha et al., 2014)

2.5. Conclusion

We suggested the combined technique of IAAL and the multi-spark discharge method for achieving the large-area fabrication of multiscale multidimensional NPSs, which allows us to uniformly produce the 3D NPSs over a large area of 50 mm x 50 mm. The size distributions and the morphologies of the nanoparticles generated by the multi-pin SDG were investigated with respect to the flow rate. We also studied the effects of the number of pins and the distance between the ground electrode and the sample on the uniformity. Then, we remarkably improved the uniformity of the 3D NPSs from less than 32% (the single-pin SDG) to above 95% (the multi-pin SDG). Plus, the capability of this technique to control the shapes and the morphologies of the 3D NPSs was proved by changing the particle sizes and the deposition time, which enables us to create various 3D NPSs even with the same pre-patterned sample. Lastly, we showed the feasibility of the large-scale assembly method by realizing the 3D back reflectors showing superior performance relative to the 1D and 2D back reflectors fabricated by the conventional fabrication method.

Chapter 3.

Electron-Beam Sintering Method of Nanoparticle Structures and its application

3.1. Introduction

Fascinating properties (Lakes et al., 1993; Ko et al., 2008; Yusko et al., 2011) arising from complex geometries of multicalc and multidimensional structures have received considerable attention in diverse fields such as electronics (Ye et al., 2004; Tseng et al., 2007), optics (Henzie et al., 2007; Rogers et al., 1999), and biosensing (Jung et al., 2014). As a part of studies in those emerging fields, various fabrication methods of multiscale composite structures have been introduced (Lee et al., 2011; Nie et al., 2008; Carlson et al., 2012; Bae et al., 2014). Much progress has been made through diverse top-down (Xia et al., 1998; Guo et al., 2007; Gates et al., 2005; Suh et al., 2009) and bottom-up (Meitl et al., 2005; Whitesides et al., 2002; Matsusaki et al., 2012; Xie et al., 1996) approaches. And, hybrid approaches (Lee et al., 2011; Cheng et al., 2006; Rahmawan et al., 2010; Yeong et al., 2004) combining the two routes or other methods have been also constantly discovered, and create a synergy effect.

Among those researches, nanoparticle-assembly techniques utilizing various fundamental external forces (Y. Min et al., 2008) including electrostatics (H. Fudouzi et al., 2002; H. Kim et al., 2006; T. J. Krinke et al., 2002; W. Prost et al., 1998), magnetic (H. Wolf et al., 2005; A. F. Demirors et al., 2013), and capillary forces (Y. Lin et al., 2003; T. Kraus et al., 2007) are potential candidates as fundamental methods to construct complex-shaped multiscale structures having useful functionalities. Especially, as already demonstrated in many researches (Kim et al., 2006;

Lee et al., 2009; Lee et al., 2010; You et al., 2010; Woo et al., 2011; Kim et al., 2011; Jung et al., 2014), ion assisted aerosol lithography (IAAL) has nanoscale controllability regarding positioning of nanoparticles on the desired locations and structuring of nanoparticles into multiscale and multidimensional nanoparticle structures (NPSs) on conductive/non-conductive substrates, which is challenges for the other methods. Moreover, there is no material constraint in this technique. In addition to those strong points, the feasibility of IAAL for novel nanodevices has been already demonstrated by fabricating three-dimensional (3D) surface-enhanced Raman scattering (SERS) substrates based on the 3D NPSs, which shows higher performance than others using 1D and 2D structures (Jung et al., 2014). However, the NPSs constructed by IAAL are easily damaged by external forces, which is an obstacle to expand applications more.

With this motivation, a new method was proposed for improving mechanical durability of the multiscale and multidimensional NPSs by sintering process using electron beam (e-beam). We also investigated changes in physical properties of the NPSs with respect to irradiation conditions of the e-beam. Moreover, using partial morphological changes in the NPSs via the e-beam, we developed a creative technique to produce various nanostructures with novel morphologies which are hard to be realized based on the conventional approaches.

3.2. Background Knowledge for Research

3.2.1. Operating Principles of E-Beam Irradiation System

Herein, the e-beam was utilized as the heating source of the sintering. In order to control the intensity of the irradiated e-beam, we adjusted experimental parameters including current, acceleration voltage, exposed time, and exposed areas. Therefore, understanding of a principle of the e-beam irradiation is required for this study. For that reason, the principle will be firstly introduced as follows.

The column of SEM consists of an electron gun, condenser lenses, deflection coils, apertures, and an objective lens (=final lens) as illustrated in figure 3.1. The electrons produced from the electron gun are converged from the cone-shaped e-beam into a spot by the condenser lenses. By adjusting the location which the initial convergence occurs, the diameter of the e-beam can be tuned, which affects the final size of the spot. And the deflection coils control the direction of the e-beam to make a zig-zag pattern on the specimen surface. Depending on the size of the apertures, the e-beam can be narrowed. Lastly, the objective lens focuses the e-beam onto the specimen. That is, the current of the e-beam irradiated onto the specimen is determined by the condenser lenses and the size of the used aperture. The voltage between the cathode and the anode which is called accelerating voltage is also one of the crucial conditions which determine the sintered extent of the NPSs. As illustrated in figure 3.2, the accelerated e-beam penetrates the specimen, and the penetration depth is dependent on the materials and the accelerating voltage. Within the region exposed by

the e-beam (called interaction volume), the kinetic energy of the accelerated e-beam is transferred to the thermal energy through collisions with atoms in the specimen. Therefore, the NPSs within the interaction volume are directly sintered via the transferred thermal energy. Additionally, the irradiated area via the e-beam can be controlled by adjusting the magnification of SEM.

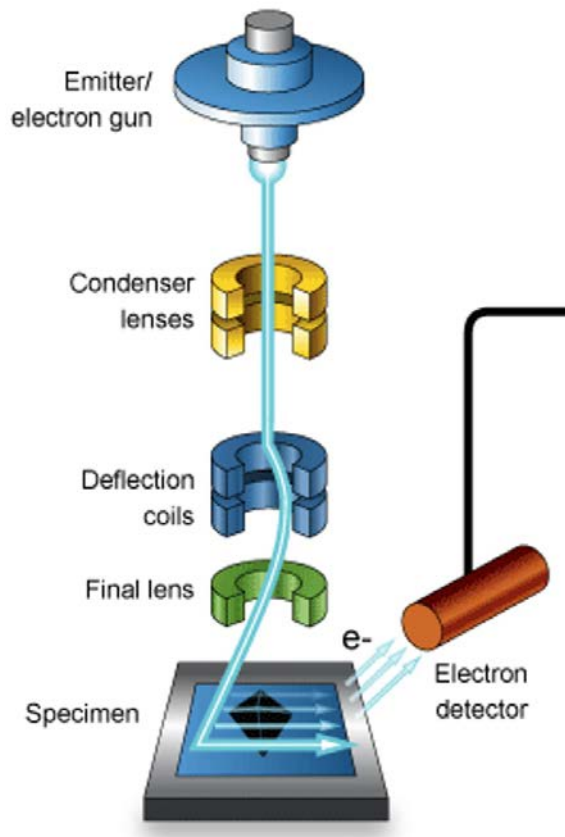


Figure 3.1. Schematic illustration of the inner structure of the SEM column (adapted from the website of Australian Microscopy & Microanalysis Research Facility)

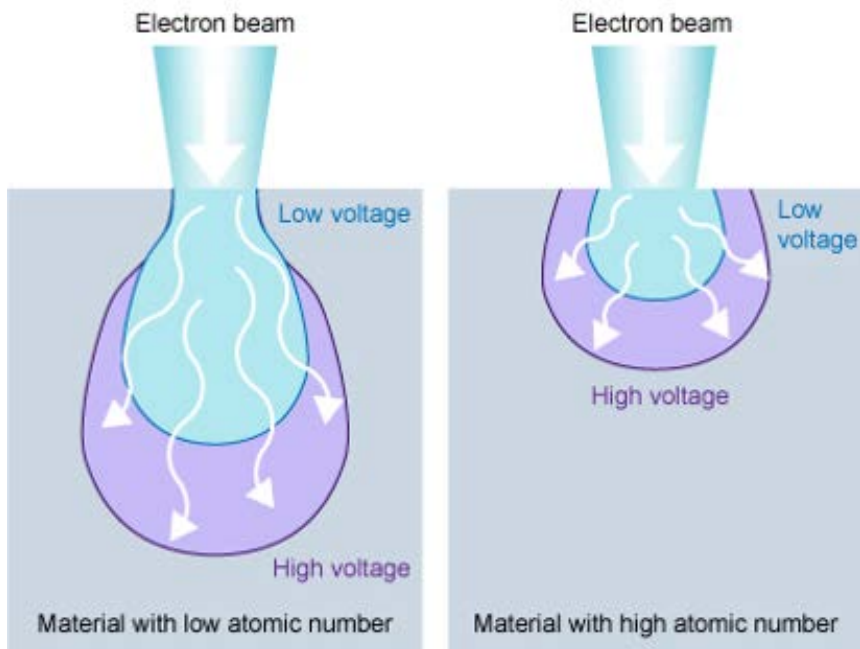


Figure 3.2. The distributions of the e-beam within the specimen depending on the acceleration voltage and the specimen type (adapted from the website of Australian Microscopy & Microanalysis Research Facility)

3.2.2. Sintering by Joule's Heating

As written in the previous section, the NPSs are directly heated by the e-beam within the interaction volume. For conductive NPSs, they are also sintered by joule's heating resulting from the current flow through the nanoparticles. Therefore, the sintering process via the e-beam is based on two principles: the thermal energy induced by the kinetic energy of the accelerated e-beam and Joule's heating. In this section, the Joule's heating will be explained.

Because Joule's heating increases temperature of nanoparticles, the Joule's heating can be used as a fusion method for changing aggregated nanoparticles into solid nanostructures in nanoscience. (Tsong et al., 1991; Barsotti et al., 2007; Bernard et al., 2007; Yilmaz et al., 2014) At the particle-particle and particle-surface interfaces, the Joule's heating can be estimated using the model shown in figure 3.3. The increase in particle temperature (Yilmaz et al., 2014) is determined by

$$\Delta T = \frac{Q}{v \cdot c_{v,p}}$$

where v is the particle volume, $c_{v,p}$ is the specific heat capacity, and the Joule's heating is

$$Q = I_p^2 \cdot R_c \cdot t$$

where I_p , R_c , and t represent the current passing through nanoparticles, the contact resistance at the particle-particle and particle-surface interfaces, and the time period, respectively. And, the contact resistance is determined by

$$R_c = \frac{\rho_c \cdot z_0}{A_c}$$

where ρ_c is the resistivity of the material at the contact, z_0 is a distance between nanoparticles, and $A_c = \frac{a^2}{r}$ is the contact area. At nanoscale dimensions, the nanoparticles are plastically deformed by van der Waals force (Maugis et al., 1984), and show the higher resistivity than the bulk material (Durkan et al., 2000; Ramsperger et al, 2001; Calleja et al., 2001; Zou et al., 2009). Based on those features of the nanoparticles, we can determine the contact radius and the contact resistance. Therefore, the ΔT due to the Joule's heating can be calculated by

$$\Delta T = \frac{3I_p^2 r \rho_c z_0 t}{4\pi c_{v,p} a^2 r^3}$$

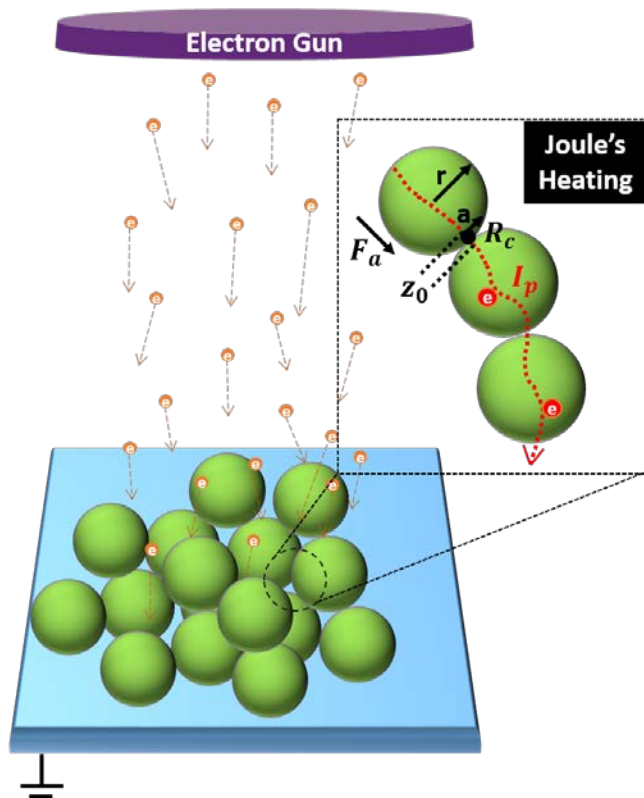


Figure 3.3. Schematic illustration of a model for the calculation of Joule's heating at the particle-particle and particle-surface interfaces.

3.3. Results and Discussion

We investigated variations in physical properties of NPSs during the e-beam sintering process. The e-beam with the accelerating voltage of 2 kV and the current of 185 pA was irradiated over the area of $0.7 \mu\text{m}^2$. Using SEM, we simultaneously measured the top-view 3D NPSs at each moment for observing the changes in the surface morphologies as time passes. In figure 3.4 (a) to (d), it was verified that the e-beam sinters the NPSs.

Unlike bulk materials, the melting temperature of nanoparticles relies on the size of the nanoparticles, and becomes lower with decreasing the particle size (Ko et al., 2007). Because NPSs via IAAL are produced by assembling nanoparticles, the melting temperature of the NPSs is dependent on the size of the nanoparticles. Therefore, NPSs consisting of small-size nanoparticles (figure 3.5) start to melt earlier than NPS consisting of large-size nanoparticles (figure 3.4). As shown in figure 3.4 and 3.5, the different results between the two NPSs reveal that the melting extent of the NPSs is determined by the size of the nanoparticles. Even under the same irradiation condition, the NPSs consisting of small-size nanoparticles (figure 3.5) was deformed more than the case of figure 3.4.

As written in chapter 2, the porosities of the NPSs can be adjusted by changing the size of the building block, because the NPSs comprise the assembled nanoparticles. Therefore, denser NPSs can be constructed with decreasing the particle size. Apart from this approach, we discovered a new way using e-beam for tuning the porosities of the NPSs. The cross-section

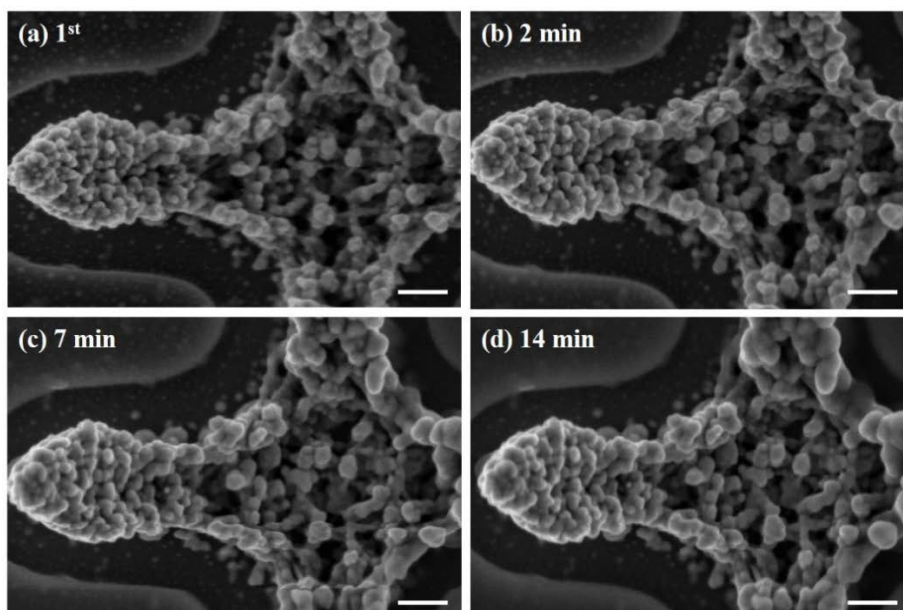


Figure 3.4. The Change in the surface morphology of the NPS as time passes. The scale bar is 100 nm in length.

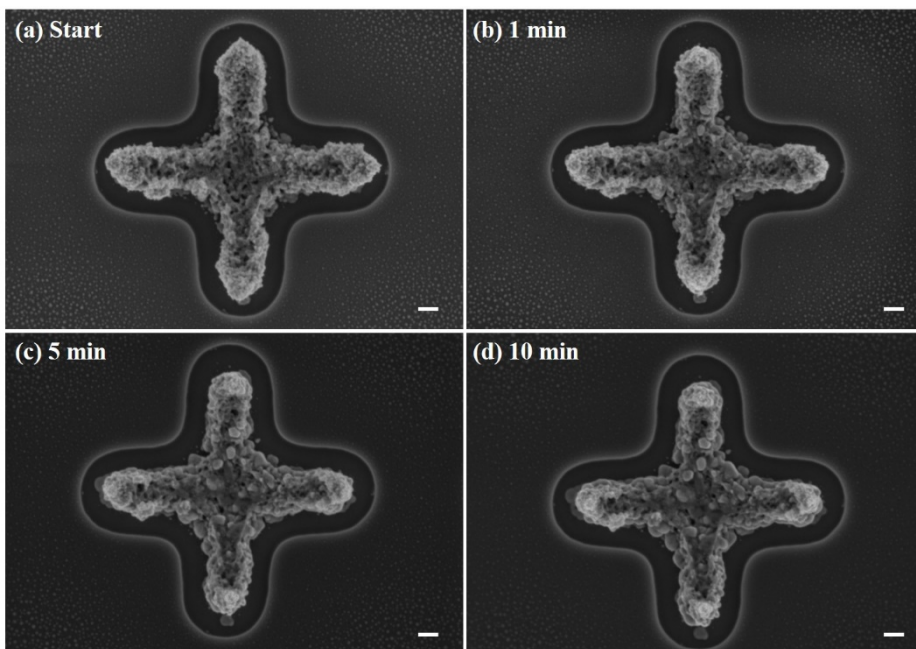


Figure 3.5. The Change in the surface morphology of the NPS as time passes. The scale bar is 100 nm in length.

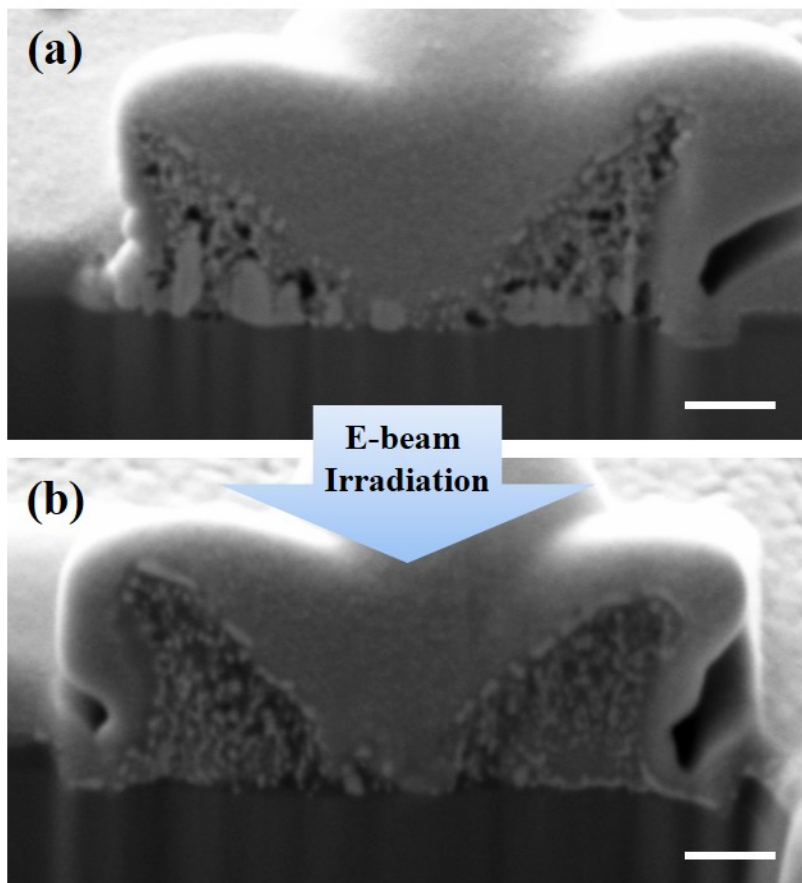


Figure 3.6. The variation in the porosity of the NPS via the e-beam irradiation: (a) before and (b) after e-beam treatment. All scale bars are 200 nm in length.

images in figure 3.6 show the variation in the porosity of the NPS. Here, the accelerating voltage of 10 kV and the current of 10 μA were applied over the area of 88 μm^2 for 1 min. The pores within the NPS are removed by the sintering process as shown in figure 3.6 (b). This result represents that the e-beam sintering technique has the capability of controlling the porosities of the NPSs.

From a different point of view, the result in figure 3.6 also exhibits an increased in stiffness of the NPSs via the e-beam irradiation. To verify the improved rigidity of the NPSs, we conducted a rigidity test by mechanical agitation using an ultrasonic bath colloquially known as a sonicator. Firstly, 3D NPSs were produced by IAAL over a large area using the multi-pin SDG as shown in figure 3.7 (a). Then, the e-beam was partially exposed using a conductive mask with the SNU-shaped opening as seen in figure 3.7 (b) under the condition (the accelerating voltage of 10 kV, the current of 30 μA , and for 15 min). As a next step, for half an hour, the sample having the sintered 3D NPSs was sonicated with the power of 200 W and the frequency of 40 kHz. Figure 3.7(c) indicates the actual image of the sample after the sonication process. Only the rainbow-colored letters of SNU were remained, which corresponds to the region where the e-beam was irradiated. The difference between figure 3.7 (d) and (e) represents the effect of the e-beam irradiation on the mechanical durability of the 3D NPSs. Figure 3.7 (d) shows the 3D NPSs in the region exposed by the e-beam. The sonic agitation did not cause any obvious changes in the 3D NPSs. However, for the case of the 3D NPSs in the region where the e-

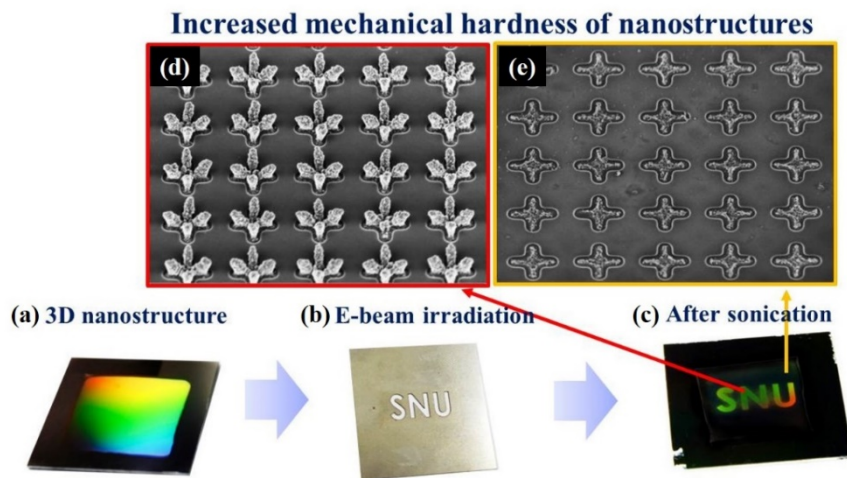


Figure 3.7. Rigidity test of the 3D NPSs sintered by the e-beam. (a) Fabrication of the 3D NPSs via IAAL. (b) Selective irradiation of the e-beam onto the 3D NPSs using a conductive mask having openings. After the sonication process: (c) the actual image of the sample, (d) the 3D NPSs in the region exposed by the e-beam, and (e) the 3D NPSs in the region where the e-beam wasn't irradiated.

beam wasn't exposed, they were disappeared after the sonication process. Because the nanoparticles are assembled by van der Waales force, the NPSs consisting of nanoparticles is easily destroyed by external forces. Therefore, this e-beam sintering technique can expand the applicability of the multiscale and multidimensional NPSs for numerous fields such as photovoltaics, sensors, and electronics.

Moreover, we observed variations in electrical properties of NPSs with increasing the power of the e-beam. As written in the previous section, nanoparticles as components of the NPSs are gradually linked by the e-beam sintering process. That is, the aggregated nanoparticles are fused into the solid-type NPSs, which results in an increase in the electrical conductivity of the NPSs. It was confirmed by the current-voltage (I-V) curves measured by conductive atomic force microscopy (AFM) as depicted in figure 3.8 (a). The same 3D NPSs are treated by the e-beam with three conditions: no treatment (reference); the accelerating voltage of 10 kV and the current of 400 nA over the area of 3.52 mm² (condition 1); the accelerating voltage of 30 kV and the current of 22 μA over the area of 0.000352 mm² (condition 2). The increased slopes of the I-V cureves in figure 3.8 (b) represent the decreased resistivity of the NPSs, which proves the improved electrical conductivity of the NPSs via the e-beam irradiation.

For the case of the generally used sintering method such as furnace sintering, the thermal energy is transferred into the entire sample. On the other hand, the e-beam can be selectively irradiated onto the sample with adjusting the magnification and/or the stage movement. That is, NPS can

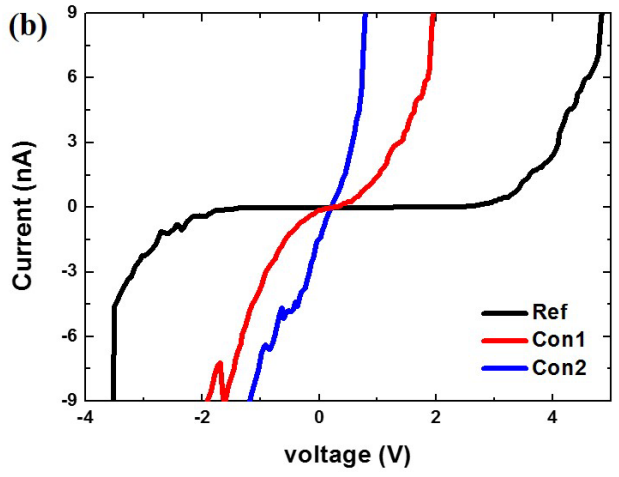
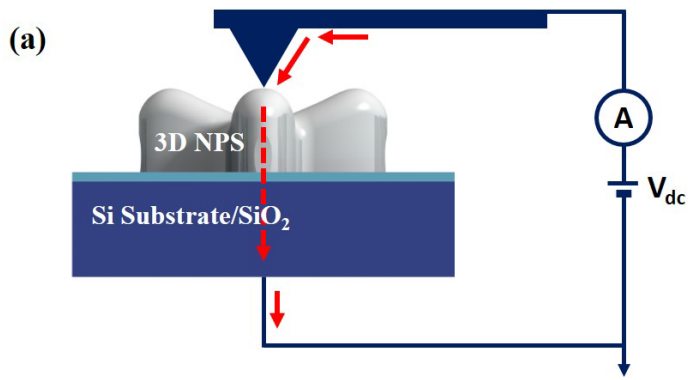


Figure 3.8. (a) Schematic illustration of the electrical measurement using conductive AFM. The red line represents the current flow. (b) I-V curves with respect to the power of the irradiated e-beam.

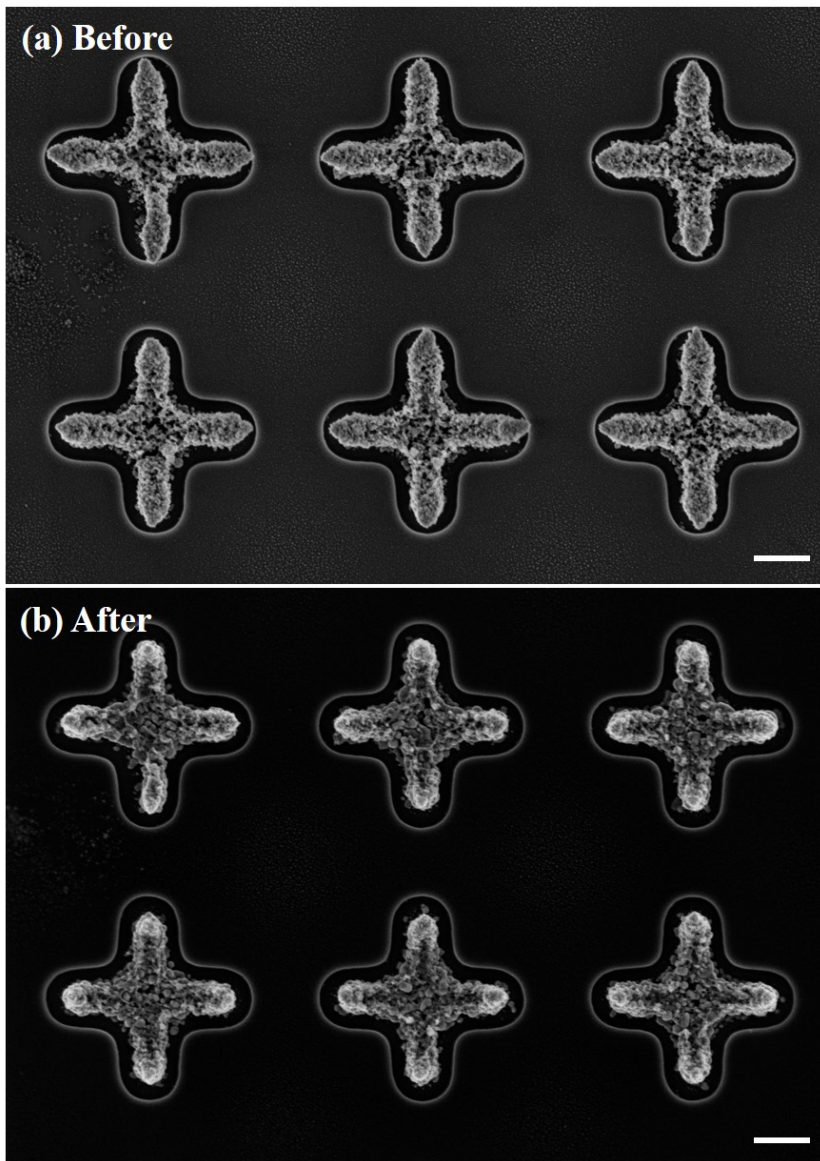


Figure 3.9. The variation in the morphologies of the NPSs through the e-beam irradiation: (a) before and (b) after e-beam treatment.

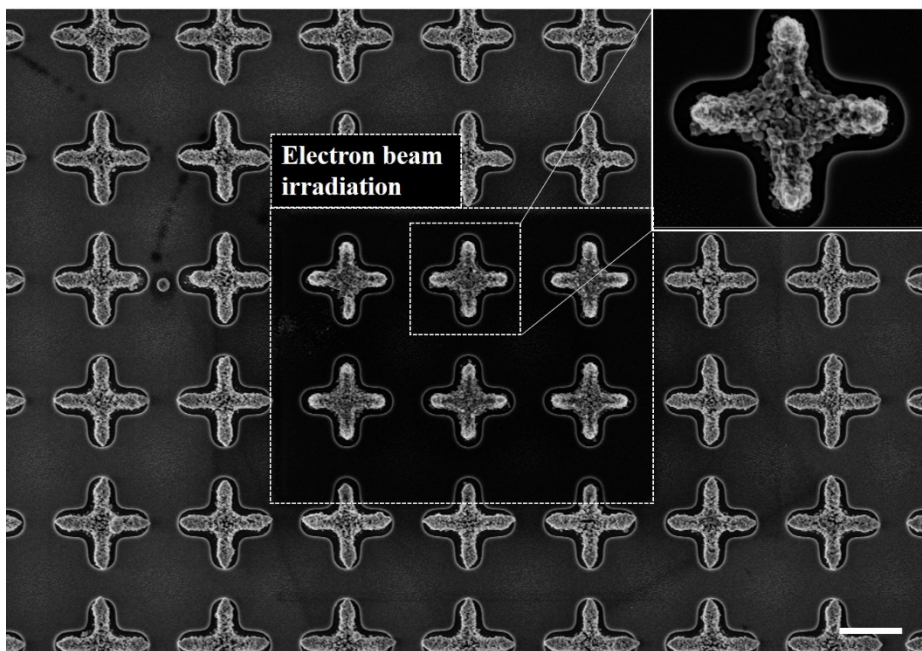


Figure 3.10. Selective sintering of the 3D NPS array. The scale bare is 1 μm in length.

be partially sintered as desired. Utilizing this strong point, many types of NPSs with various porosities, sizes, and morphologies can be produced on the same substrate. In addition, the number of the pores within the NPSs decreases with the e-beam treatment, which results in the shrinkage of the NPSs. Figure 3.9 (a) and (b) show the obvious difference of before and after e-beam treatment with the accelerating voltage of 2 kV, the current of 185 pA, and the irradiated area of $27.65 \mu\text{m}^2$ for 10 min. The smaller NPSs in the sintered region (the dotted box in figure 3.10) also verify the decrease in the entire size of the NPSs after the e-beam treatment.

Further, the shrinkage phenomenon of the NPSs was confirmed by the changes in the scattering intensities of the NPSs with increasing the e-beam intensity via a dark-field (DF) microscopy. The e-beam was irradiated onto the same NPSs with 5 conditions: conditions 1, 2, 3, 4, and 5 are the intensities of 1.14×10^{-3} , 4.13, 11.4, 34.1 and 1870 W/mm^2 , respectively. Here, the e-beam intensity was controlled by adjusting the exposed area, the accelerating voltage, and the current as summarized in Table 3.1. Figure 3.11 represents the measured scattering intensities of the NPSs. For condition 1, the peak was blue-shifted resulting from the decrease in the entire size of the NPSs compared to the reference (no exposure). The scattering intensity of the condition 2 decreased more relative to the condition 1 because the NPSs are shrunk more with larger e-beam intensity. Until the condition 5, the scattering intensities gradually become weaker, which represents the continuous shrinkage of the NPSs. From these data, it was found that this e-beam sintering technique has the capability of tuning

	Exposed Area [mm ²]	Time [sec]	V _{acc} [kV]	Probe Current [A]	Power=IV [W]	Intensity=IV/A[W/mm ²]
Con1	3.52	60	10	4.00E-07	0.00400	1.14E-03
Con2	0.001452	60	10	6.00E-07	0.00600	4.13
Con3	0.000088	60	10	1.00E-07	0.00100	11.4
Con4	0.000352	60	10	1.20E-06	0.01200	34.1
Con5	0.000352	60	30	2.19E-05	0.65700	1870

Table 3.1. E-beam irradiation conditions for the optical measurement of the 3D NPSs.

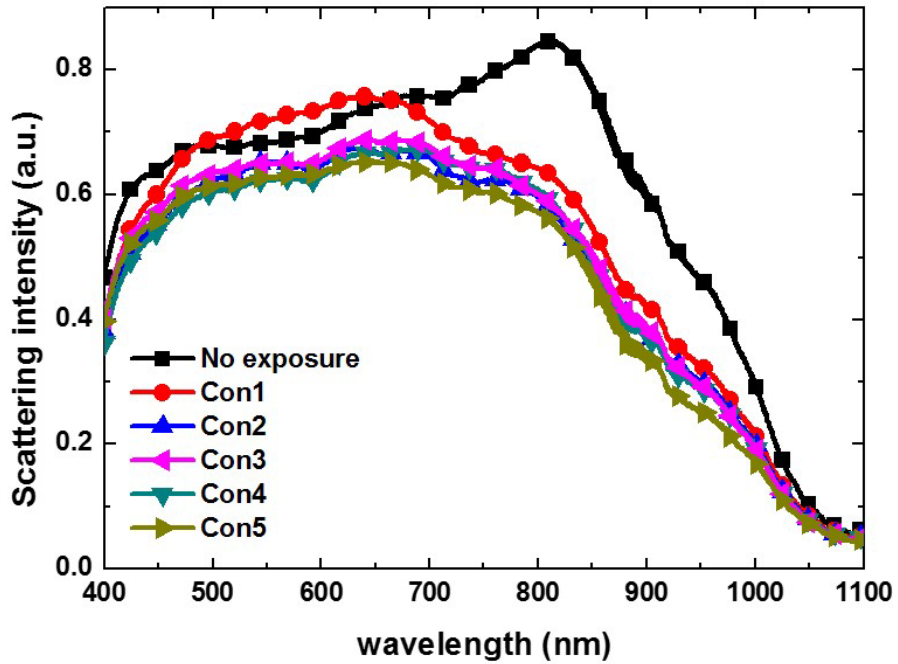


Figure 3.11. Variations in the scattering intensities of the NPSs with increasing the power of the e-beam.

optical properties of nanostructures.

Lastly, based on the shrinkage phenomenon and the selective sintering of the e-beam technique, we discovered a new route to produce 3D NPSs with novel morphologies. In order to maximize the shrinkage phenomenon, the porous 3D NPSs were intentionally constructed using somewhat large-size nanoparticles for increasing the number of the pores within the NPSs. Then, the fabricated 3D NPSs were selectively sintered by the e-beam by adjusting the magnification and the sintered location. As seen in figure 3.12, the asymmetric pattern was fabricated by sintering the entire NPS at the center and a half or a quarter of the NPSs surrounding the NPS at the center.

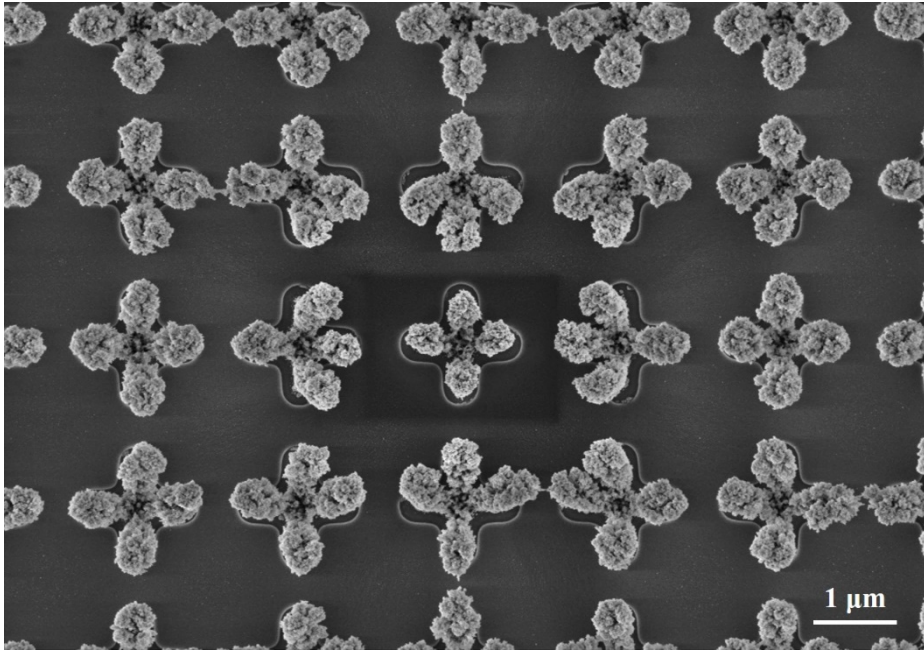


Figure 3.12. Fabrication of the asymmetric pattern via the selective sintering process using the e-beam.

3.4. Conclusion

We found a new method to sinter the NPSs utilizing the e-beam. The effect of the e-beam irradiation on the surface morphologies of the NPSs was investigated with respect to the particle size, which results from the particle size dependency of the melting temperature of the NPSs. By adjusting e-beam conditions, the porosities of the NPSs can be also controlled. We further demonstrated the sintered NPSs showing the improved mechanical durability and electrical properties compared to the original structures without any treatment. Moreover, the capability of the e-beam sintering method to tune the optical properties of the NPSs was studied. Lastly, based on the unique features of the sintering technique including the shrinkage phenomenon of the NPSs and the selective exposure of the e-beam, we additionally discovered a new approach for restructuring the NPSs with novel morphologies. In addition to the large-area patterning in chapter 2, the e-beam sintering method in this chapter provides many chances for the use of the mulicale and multidimensional NPSs for numerous applications. Furthermore, this technique has the huge potential for fabricating various and unique patterns which is hard to be realized based on the conventional techniques.

Chapter 4.

Thin-Film Si Solar Cell incorporating 3D Nanoparticle Structures

4.1. Introduction

In terms of achieving thin-film solar cells with high power conversion efficiency, light trapping schemes using nanostructures have been considered as promising candidates. Recently, multiscale three-dimensional (3D) nanostructures have attracted widespread interest in the field of photovoltaics due to the potential for 3D-nanostructure-induced absorption enhancement in a multi-spectral range. (Guldin et al., 2010; Ko et al., 2011; Yu et al., 2011; Kwon et al., 2014) However, most studies have focused on simple-shaped nanostructures including nanoparticles, nanowires, gratings, and nanobumps (Awater et al., 2010; Baek et al., 2014; Chen et al., 2014; Garnett et al., 2010; Liu et al., 2014; Meskamp et al., 2012; Ferry et al., 2010; Zhu et al., 2010; Ferry et al., 2011; Deceglie et al., 2012, Hsu et al., 2012; Mihi et al., 2014) because of technical difficulties in employing the 3D nanostructures to solar cells, especially inorganic thin-film solar cells. Therefore, a new approach is required for utilizing the 3D light trapping structures to inorganic thin-film solar cells. For an effective and practical use of 3D nanostructures in these solar cells, the approach is expected to meet several demands including nanoscale-resolution controllability of physical dimensions, wavelength tunability, reproducibility, and wafer-scale production. Ion assisted aerosol lithography (IAAL) (Kim et al., 2006; Lee et al., 2009; Lee et al., 2010; You et al., 2010; Woo et al., 2011; Kim et al., 2011; Jung et al., 2014) is highly regarded as an efficient way in fulfilling these requirements. By

means of a combination of IAAL and a multi-spark discharge method (Ha et al., 2014; Han et al., 2012), 3D nanoparticle structures (NPSs) can be uniformly constructed in a parallel fashion at room temperature and atmospheric pressure.

Here we demonstrated thin-film hydrogenated nanocrystalline silicon (nc-Si:H) solar cells incorporating 3D NPS arrays (called 3D solar cell hereafter) based on the combined technique of IAAL and the multi-spark discharge method. The 3D-NPS-induced enhancement of light trapping was verified by investigating optical properties of Ag-coated 3D NPSs (called 3D back reflector hereafter) and 3D-textured front contact through experiments and electromagnetic simulations. The fabricated 3D solar cell showed optically and electrically superior performance compared to a flat cell and a cell on nanoparticle clusters (NPCs). Then, to support these results, the absorption in nc-Si:H of the 3D solar cell was calculated by finite-difference time-domain (FDTD) simulations over a broad spectral range from 350 to 1100 nm where nc-Si:H is optically active.

4.2. Experimental Procedure and Simulation

4.2.1. Fabrication Process for thin-film nc-Si:H solar cells

Employing 3D NPS arrays

Figure 4.1 represents a schematized fabrication flow of the 3D solar cell. For fabricating the 3D NPS array over a large area, the combined approach of IAAL and the multi-spark discharge method was utilized. The schematic of the multi-spark discharge device for generating charged nanoparticles was introduced in chapter 2. Both positive ions generated by corona discharge process and positively charged nanoparticles produced by spark discharge process are widely injected toward a Si substrate along carrier gas of nitrogen. With the negatively biased substrate, the positive ions first arrive at the Si substrate due to their larger electrical mobility than charged nanoparticles, and the ions are accumulated on a surface of an insulating SiO₂ film, which repels the following positively charged nanoparticles. Also, the distorted equipotential surfaces resulting from the accumulated ions act as a nanoscopic electrostatic lens near each opened region of the SiO₂ film. Therefore, the positively charged nanoparticles are focused within the exposed regions of the Si substrate in a parallel manner as illustrated in figure 4.1 (a). The distorted shape of the equipotential surfaces and the antenna effect originating from adjacent 3D NPSs critically influence the final morphology of the 3D NPSs. Detailed information of IAAL (Kim et al., 2006; Lee et al., 2010; Woo et al., 2011; Kim et al., 2011; You et al., 2010; Lee et al., 2009, Jung et al., 2014) and

the multi-spark discharge method (Ha et al., 2014; Han et al., 2012) was explained in previous researches. Here, we used the cross-shaped SiO₂ pattern with 400 nm in width and 550 nm in length as depicted in the inset of figure 4.2 (a). And the 50-nm-thick SiO₂ pattern has a 2 μm period. Figure 4.2 (a) shows the fabricated 3D NPS array used as a template of the 3D solar cell. As a next step, in order to minimize defects in the nc-Si:H layer caused by valleys of the rough surface of the substrate, (Hsu et al., 2012; Li et al., 2009; Python et al., 2009) undercuts between the 3D NPS and the SiO₂ pattern were filled by spin-on-glass (SOG) coating process as depicted in figure 4.1 (b). The 3D NPSs with rounded edges (see figure 4.2 (e) and (f)) stemming from surface tension of the SOG play a critical role to enhance light trapping effect and to reduce deterioration of electrical outcomes of the 3D solar cell. Then, a 300-nm-thick Ag back electrode was deposited on the 3D NPS array at an oblique angle via thermal evaporation process for achieving the conformal Ag film along with the surface morphology of the 3D NPSs (figure 4.1 (c) and 4.2 (b)). As seen in figure 4.1 (d), a 130-nm-thick aluminum-doped zinc oxide (ZnO:Al) layer was sputtered on the Ag-coated 3D NPSs followed by the deposition of the nip nc-Si:H stack with a 500-nm-thick intrinsic layer by plasma-enhanced chemical vapor deposition. Lastly, an 80-nm-thick indium tin oxide (ITO) front contact was sputtered. Scanning electron microscope (SEM) images in figure 4.2 (c-f) show the tilted and cross-section views of the 3D solar cell. All thin-film nc-Si:H solar cells in this study were produced at the same condition.

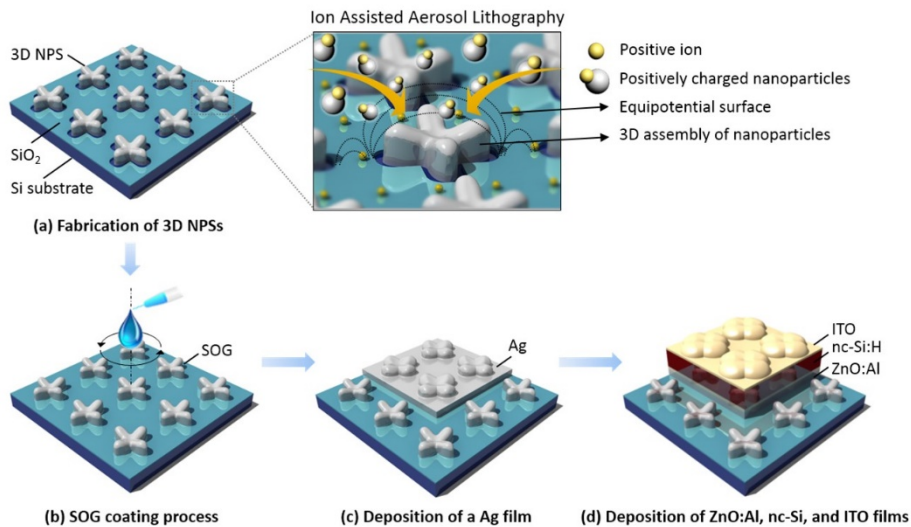


Figure 4.1. Schematized process of manufacturing a 3D solar cell (a) 3D NPSs (NPSs) used as a template of the 3D solar cell are uniformly constructed via ion assisted aerosol lithography (IAAL) on a Si substrate. The inset reveals the process of IAAL: the yellow arrow represents the direction of charged nanoparticles migrating along with the distorted equipotential surfaces induced by accumulated positive ions on the surface of the SiO₂ film. (b) Spin-on-glass (SOG) coating process for eliminating the undercuts between the 3D NPSs and the SiO₂ film. The 3D solar cell is produced by depositing (c) Ag, (d) ZnO:Al, nc-Si:H (nip configuration, an intrinsic layer = 500 nm), and ITO films on the 3D NPS array.

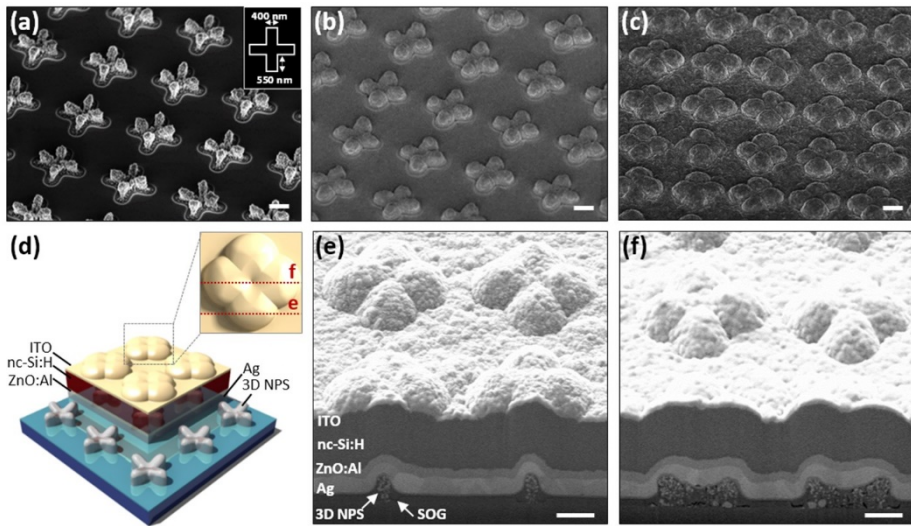


Figure 4.2. SEM images indicating each fabrication process for the 3D solar cell: (a) 3D NPSs fabricated on the Si substrate and the physical dimension of the used SiO₂ pattern in the inset; (b) Ag-coated 3D NPSs called 3D back reflector (BR) in this study; (c) the tilted view of the 3D solar cell. (d) Schematic illustration of the 3D solar cell. (e, f) SEM images of each cross section of the 3D solar cell. All scale bars are 500 nm in length.

4.2.2. Setup for FDTD simulations

Herein, in order to study the optical properties of the 3D back reflector (BR) and the 3D solar cell, electromagnetic modeling was carried out using Lumerical FDTD simulation software. The simulation model is based on measured results via SEM and atomic force microscopy (AFM) as seen in tables 4.1. and 4.2. The refractive indexes of the ZnO:Al, nc-Si:H, and ITO films were taken from spectroscopic ellipsometry measurements. And, the experimental data of Palik (Palik et al., 1998) was utilized as the refractive index of Ag. Because the 3D NPSs are arrayed with a period of 2 μm , the 3D BR and the 3D solar cell were calculated over a 2 μm x 2 μm region with periodic boundary conditions in the 350- to 1100-nm spectral range.

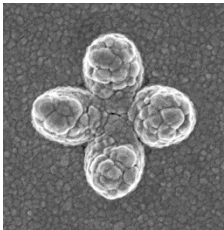
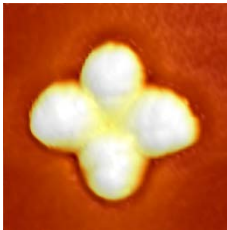
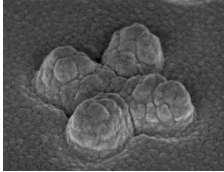
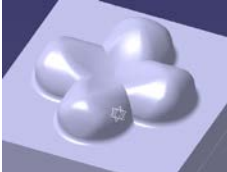
3D BR	SEM	AFM	Simulation model
Top view			
Tilted view			

Table 4.1. Top and tilted views of the 3D BR measured by SEM (left) and AFM (middle). Simulation model (right) of the 3D BR using CATIA.

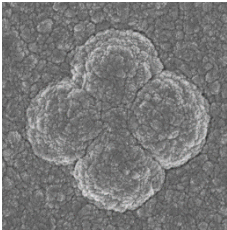
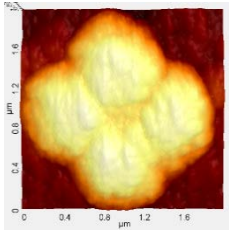
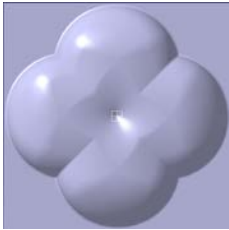
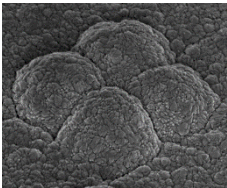
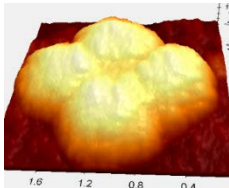
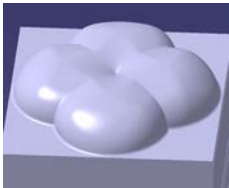
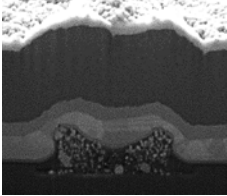
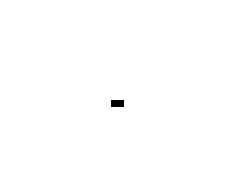
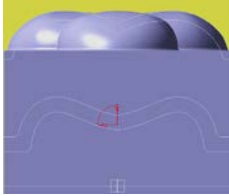
	SEM	AFM	Simulation model
Top view			
Tilted view			
Cross section			

Table 4.2. Top, tilted, and cross-sectional views of the 3D solar cell measured by SEM (left) and AFM (middle). Simulation model (right) of the 3D solar cell using CATIA.

4.3. Results and Discussion

4.3.1. Optical Properties of the 3D BR

Firstly, we characterized optical properties of the 3D BR. Plasmonic structures reveal enhanced scattering and absorption features at surface-plasmon-resonance wavelengths, and they illuminate same colors as those at the resonance wavelengths. (Maier et al., 2005) As shown in figure 4.3 and 4.4, multiple plasmon resonances of the multiscale 3D BR were verified by multiple peaks of diffuse reflectance (DR) via UV-Vis-NIR spectrophotometer (Cary 5000, Agilent Technologies) and multiple colors of a dark-field (DF) image via DF microscopy (an optical microscopy and a CCD camera are BX51 and DP73, respectively, Olympus). Additionally, the improved scattering property of the 3D BR was observed over a broad spectral range from 300 to 1100 nm (see figure 4.3), which results from the multiple plasmon resonance effect and multiscale roughness of the Ag film with 3D nano/micro composite structures. These features increase the optical path length and the electric field intensity within the nc-Si:H layer, leading to an enhancement in absorption of the 3D solar cell.

In this study, each 3D NPS constructed by IAAL has various dimensions from nano- to micro- scales in x, y, and especially z directions as illustrated in figure 4.4. (a), which is unavailable through conventional fabrication methods due to technical difficulties and/or complicated fabrication procedures. To emphasize this advantage of the 3D NPS via IAAL and to confirm the existence of the multiple plasmon resonances, 3D

electromagnetic modeling was performed using numerical FDTD simulation software for calculating profiles of electric field intensities of the 3D BR along the z axis. Figure 4.5 (b-d) show the calculated results of the electric field intensities at the multiple peaks of the DR in figure 4.3 ($\lambda_1 = 450$, $\lambda_2 = 580$, and $\lambda_3 = 800$ nm). We observed localized resonances near the 3D BR demonstrating the surface plasmon resonance phenomenon which causes the enhanced scattering and absorption effects. And, at each wavelength, the positions of the localized resonances near the 3D BR correspond well with the colors of the DF image representing resonance wavelengths.

Moreover, the superior optical performance of the 3D BR was proved by comparison with those of the flat Ag film (called flat BR hereafter) and the BR employing randomly distributed nanoparticle clusters (NPCs). The NPCs were prepared by spin-coating process of silica nanoparticles with 200 nm diameter equivalent to the minimum dimension of the top-view 3D NPS. Here, percentages of area coverages of the 3D NPSs and the NPCs were fixed at approximately 12% (see figure 4.6). Then, the BR incorporating the NPCs (called NPC BR) was fabricated by depositing an Ag film on the NPCs through the same approach as used for the 3D BR. As shown in measured total reflectance (TR) and DR curves of the three BRs (Figure 4.3), the 3D BR reveals the best optical performance relative to those two references of the flat and NPC BRs. Even with the same percentage of the area coverage, the 3D BR shows better optical features including the TR and the DR than the other BRs. Although the rough Ag

surface of the NPC BR formed by the randomly aggregated nanoparticles leads to broadband enhanced scattering, the NPC BR exhibits weaker scattering property and larger parasitic absorption loss compared to the 3D BR, demonstrating the lower TR and DR of the NPC BR. Additionally, the useful features of IAAL ensuring precise control of structuring with nanoscale resolution, wavelength tunability, and reproducibility make the 3D BR stronger than the other BRs.

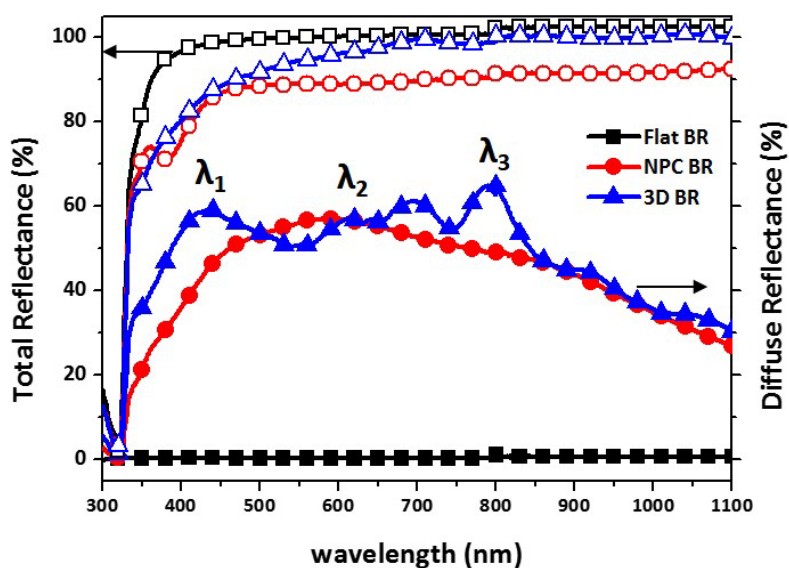


Figure 4.3. Total and diffuse reflectance (TR and DR) curves of the three-type BRs. Black (squares), red (dots), and blue (triangles) lines represent the flat, nanoparticle clusters (NPCs), and 3D BRs, respectively.

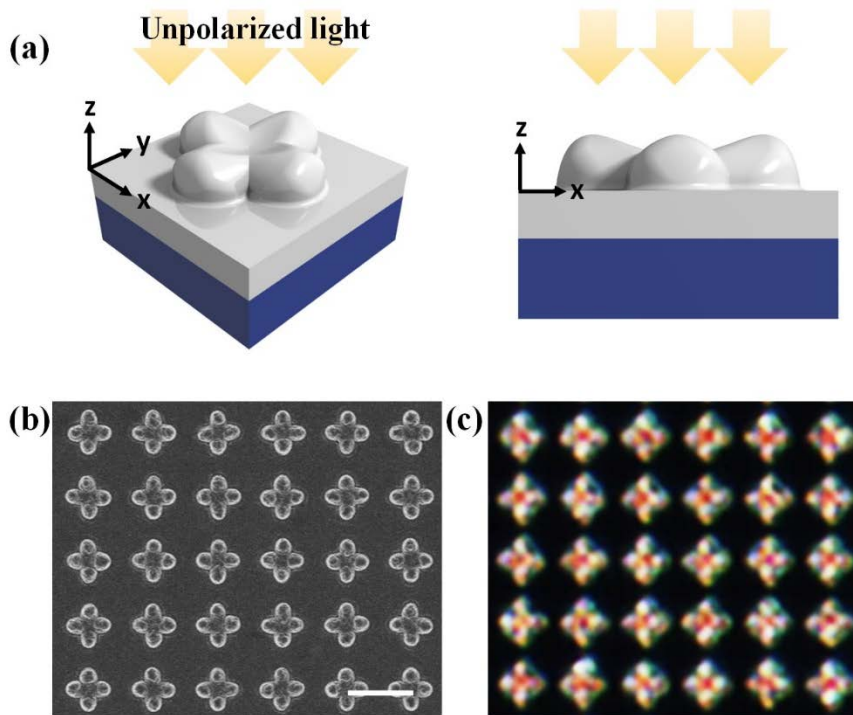


Figure 4.4. (a) Schematic illustrations of the 3D BR fabricated by three steps (fabrication of the 3D NPSs via IAAL, spin-on glass (SOG) process on the 3D NPSs, and deposition of a 300-nm-thick Ag film on the 3D NPSs). (b) SEM and (c) the dark-field (DF) images of the 3D BR (scale bar: 1 μm).

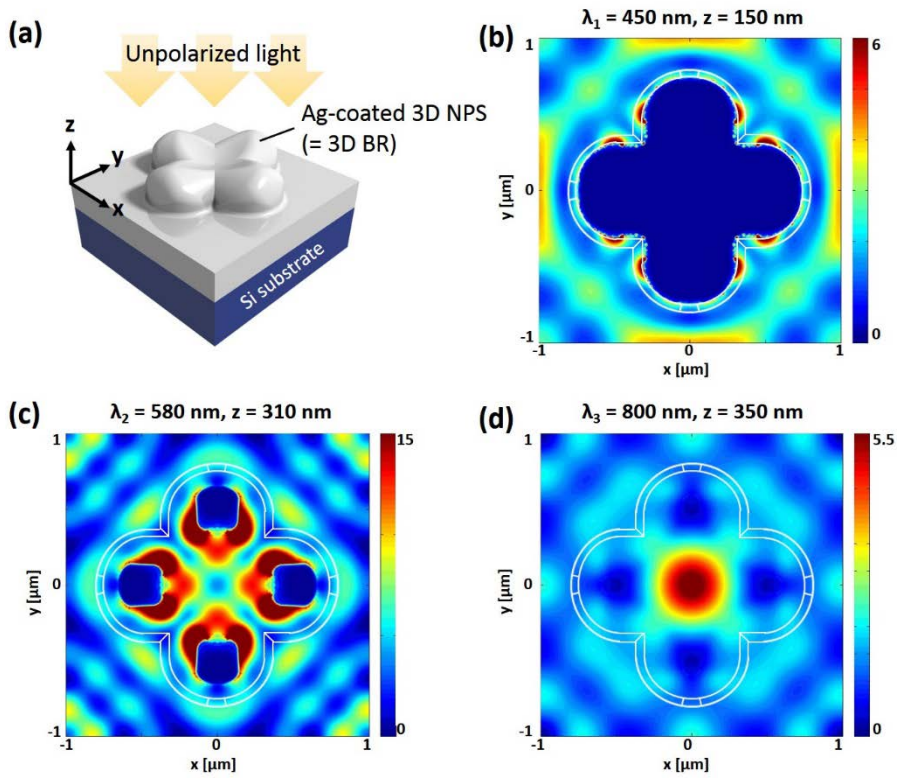


Figure 4.5. (a) Simulation model of the 3D BR. Profiles of the electric field intensities of the 3D BR at representative resonance wavelengths (λ_1 - λ_3) in the DR curve of the figure 4.3 with respect to the z axis: (b) $z=150 \text{ nm}$, (c) $z=310 \text{ nm}$, (d) $z=350 \text{ nm}$.

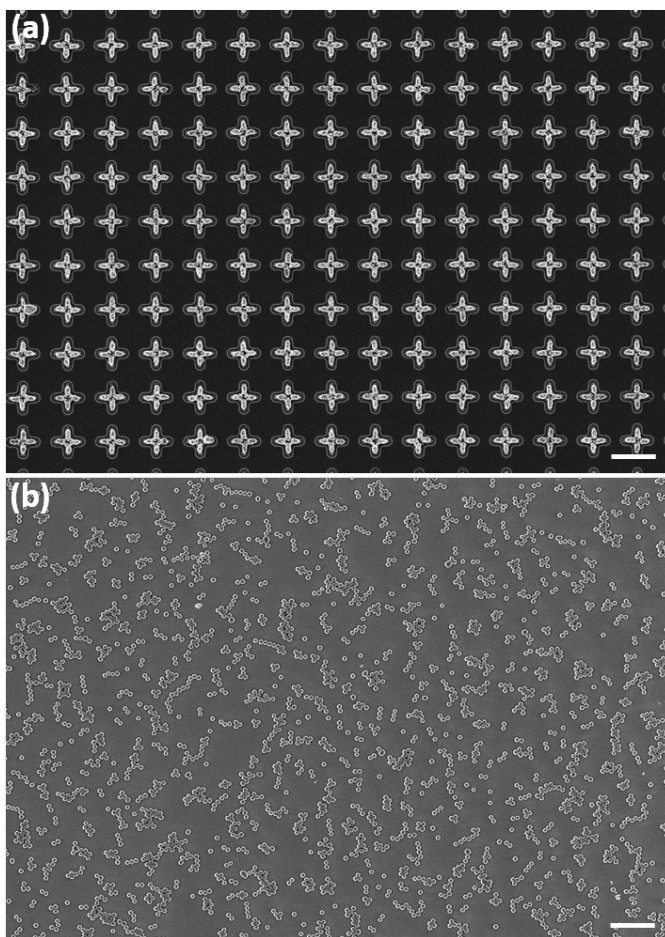


Figure 4.6. SEM images show top views of (a) the 3D NPSs and (b) the NPCs. (scale bar: 2 μm)

4.3.2. Optical and Electrical Performance of the 3D Solar Cell

As a next step, the current density-voltage (J-V) characteristics and the external quantum efficiencies (EQEs) of the three-type solar cells were measured as seen in figure 4.7, and Table 4.3 shows the summary of their performance parameters. In comparison with the flat cell, the 3D solar cell reveals a significant increase in short-circuit current density (J_{sc}), resulting in a 20% increase in the efficiency, whereas the cell employing the NPCs (called NPC solar cell hereafter) shows a 9% increase in the efficiency with a smaller increase in J_{sc} than the 3D solar cell. The different performance between the 3D and the NPC solar cells can be explained by the measured EQEs (Figure 4.7 (b)). The EQE of the 3D solar cell exhibits enhanced spectral response for wavelengths ranging from 350 to 1100 nm with higher values than the NPC solar cell. These EQEs correspond well to light absorption curves of the 3D and the NPC solar cells as seen in the inset of figure 4.7 (b). In addition, it also supports the highest EQE of the 3D solar cell that the NPC BR has the smaller DR and the larger parasitic absorption loss than the 3D BR in figure 4.3. All these improved optical properties including the reflectance, the absorption, and the EQE are consistent and account for a 30% increase in J_{sc} of the 3D solar cell.

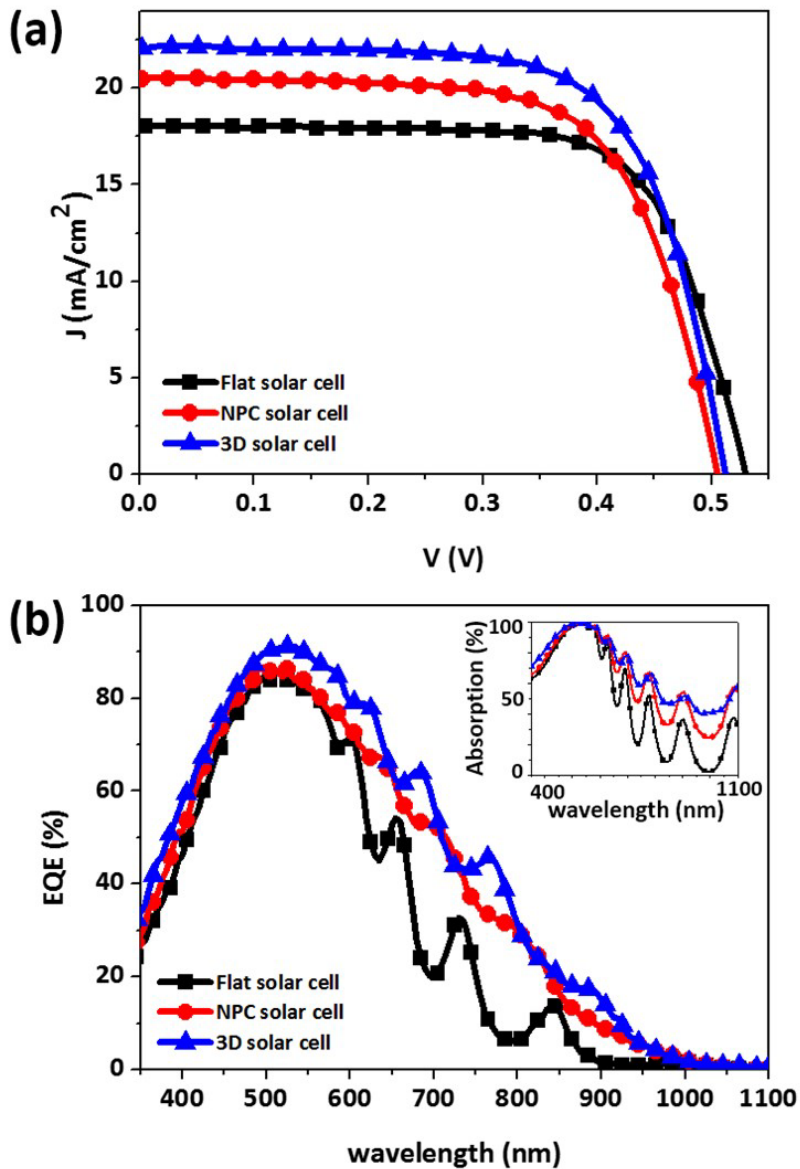


Figure 4.7. (a) Current density-voltage (J-V) curves and (b) external quantum efficiencies (EQEs) of the champion flat (squares), NPC (dots), and 3D (triangles) solar cells, absorption curves of the three cells in the inset of figure 4.7 (b).

	V_{oc} (V)	J_{sc} (mA/cm ²)	FF (%)	Efficiency (%)
Flat	0.53	17.05	70.97	6.41
NP Clusters	0.51	20.48	67.46	6.98
	3.77% ▽	20.12% ▲	4.95% ▽	8.89% ▲
3D NPSs	0.51	22.07	68.71	7.77
	3.77% ▽	29.44% ▲	3.18% ▽	21.22% ▲

Table 4.3. Summary of all electrical outcomes of the thin-film nc-Si:H solar cells fabricated in this study. Device architectures are: substrate: nothing or nanostructures (NPCs or 3D NPSs): Ag (300 nm): ZnO:Al (130 nm): nc-Si:H with a 500-nm-thick i-layer: ITO (80 nm).

4.3.3. Analysis of Enhanced Factors of the 3D Solar Cell

The effects of the interfaces of the 3D solar cell

For further understanding of the greatest outcome of the 3D solar cell herein, each role of the 3D front contact and the 3D BR was separately investigated except interference effect caused by the thickness of the nc-Si:H layer. In section 4.3.1, although the multiple plasmon resonances of the 3D BR was proved, the optical properties of the 3D BR surrounded by air was obtained due to experimental limitations for the measurement of the real system. Since optical properties of plasmonic structures are dependent on surrounding materials, (Jensen et al., 1999) FDTD simulations were carried out for calculating the scattering properties of the actual 3D BR surrounded by the 130-nm-thick ZnO:Al and infinite nc-Si:H layers as depicted in figure 4.8 (a). The refractive index of the ZnO:Al was taken from spectroscopic ellipsometry measurements, and that of Ag was based on the experimental data of Palik. (Palik et al., 1998) However, in order to investigate the scattering property of 3D BR, the imaginary part of the measured refractive index of the nc-Si:H was set to zero, and the averaged value of 3.8 was set as the real part of the refractive index of the nc-Si:H. Figure 4.8 (b) indicates the increased scattering effect over a broad spectral range and the real locations of the multiple plasmon resonances of the 3D BR, leading to the enhanced light trapping effect in the 3D solar cell. Then, the role of the 3D front contact was studied using the designed architecture in figure 4.9 (a). The calculation for the transmittance enhancement into the nc-Si:H only with the 3D front contact

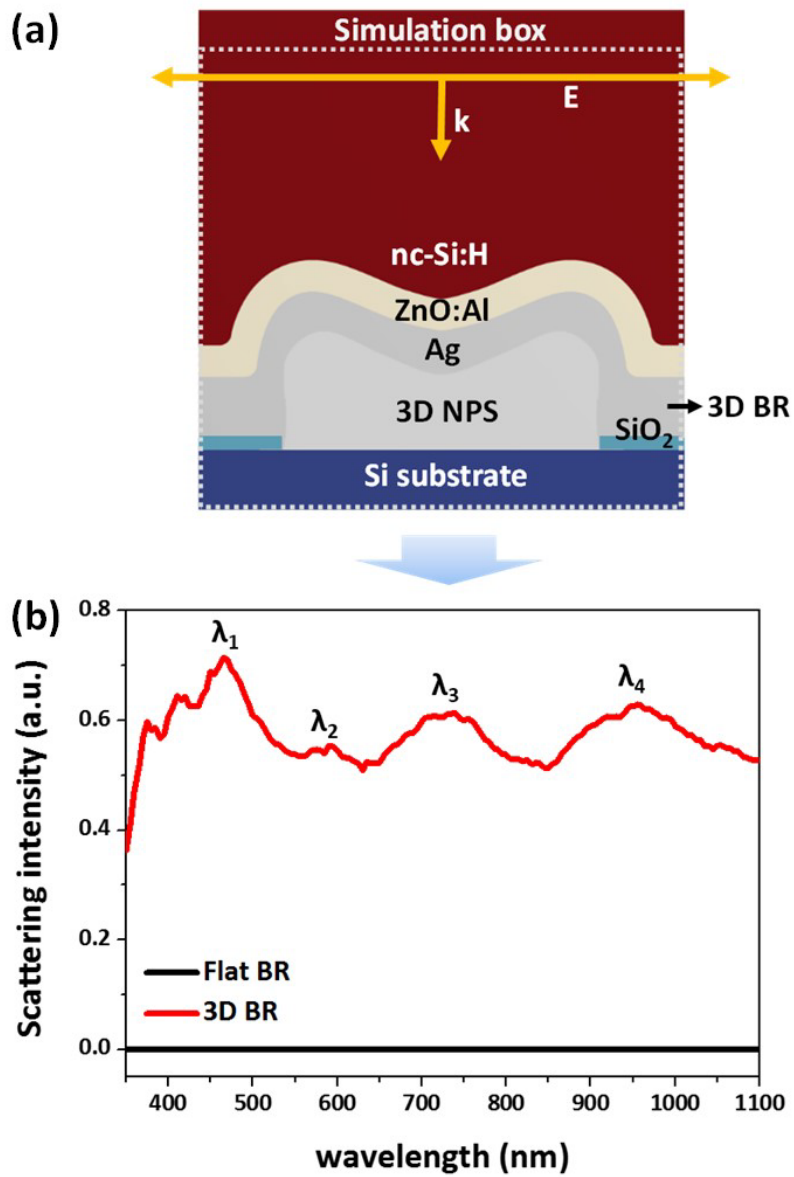


Figure 4.8. The simulated model for calculating the effect of (a) the 3D BR surrounded by the ZnO:Al/nc-Si:H layers. Calculated results of (b) scattering intensities of the flat (black line) and 3D (red line) BRs.

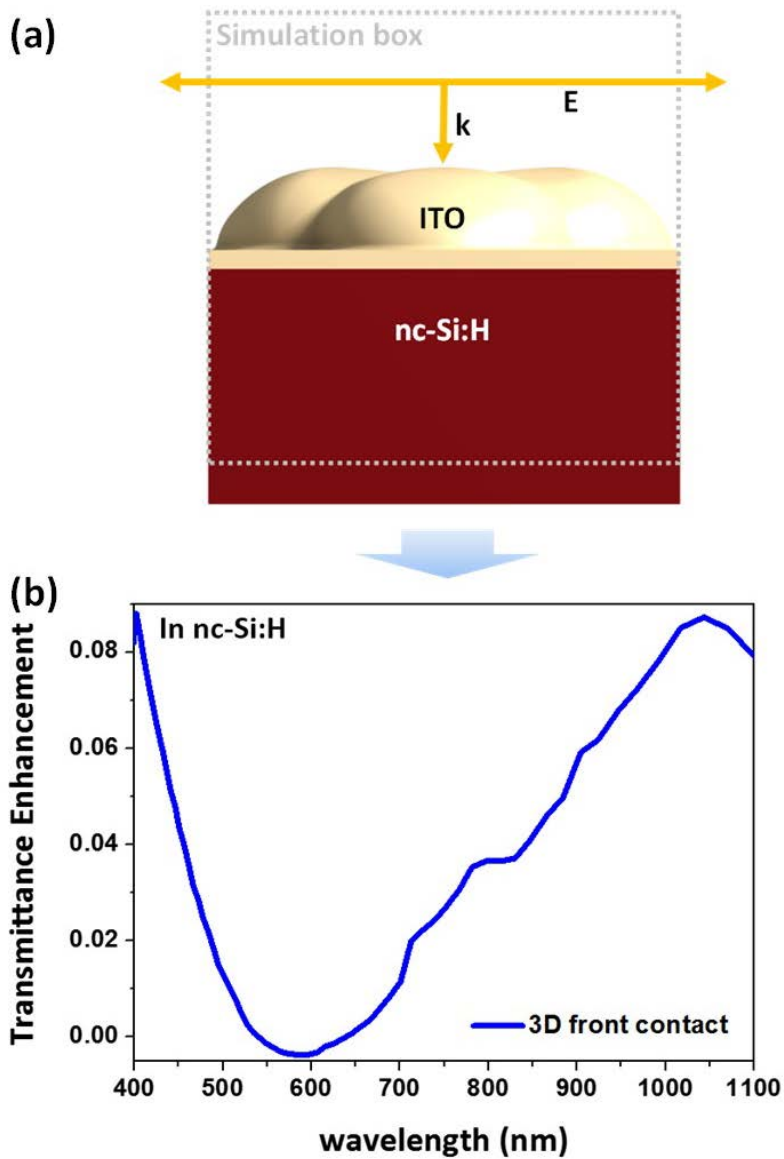


Figure 4.9. The simulated model for calculating the effect of (a) the 3D front contact. (b) Transmittance enhancement in nc-Si:H (blue line) induced only by the 3D front contact.

was performed with the measured refractive index of the ITO by spectroscopic ellipsometry and the artificially modified refractive index of the nc-Si:H (real part = 3.8, imaginary part = 0). Over a broad spectral range, the 3D front contact facilitates that more light can be transmitted into the nc-Si:H causing the enhanced absorption in the 3D solar cell, the so-called antireflection effect (see figure 4.9 (b)). Both simulated outcomes of the 3D BR and the 3D front contact support the EQE results (Figure 4.7 (b)) very well.

Optical generation rate in the nc-Si:H layer

Lastly, since the 3D front contact and the 3D BR always coexist in one 3D solar cell via the fabrication approach used in this study, the combined effects of the two must be investigated for the better understanding of the 3D solar cell. For that reason, absorption in the nc-Si:H was calculated at each wavelength over the spectral range of 350-1100 nm where the nc-Si:H is optically active using the real architecture of the 3D solar cell as depicted in figure 4.10 (a). The absorption (called carrier generation rate, $G(\lambda)$ herein) can be calculated utilizing

$$G(\lambda) = \frac{\varepsilon'' |E|^2}{2\hbar}$$

where ε'' is the imaginary part of the permittivity and E is the electric field. (Ferry et al., 2010; Ferry et al., 2011; Deceglie et al., 2011; Yaghjian et al., 2007) Here, we assume that power absorbed is converted to carriers in full, and all simulations were performed with unpolarized light source. Unlike other simple-shaped nanostructures, the 3D NPSs

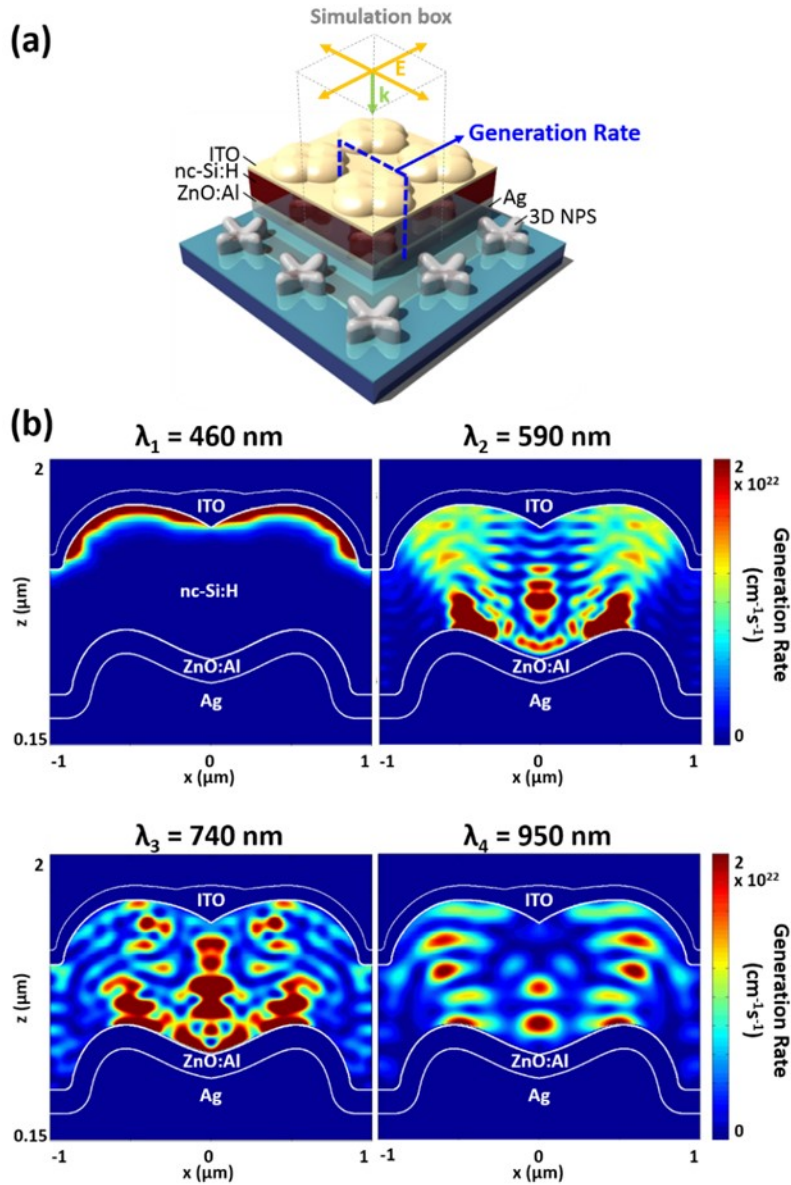


Figure 4.10. (a) Schematic illustration of the 3D solar cell for calculating the generation rate in the nc-Si:H layer. (b) Cross sections of each optical generation rate in nc-Si:H at the four wavelengths (λ_1 - λ_4 in figure 4.8 (b)) indicating the representative resonance locations of the 3D BR.

exhibit the multiple-plasmon-resonance responses yielded by the multidimensional effect of the 3D NPSs. Thus, the carrier generation rate within the nc-Si:H was observed at the representative resonance wavelengths (λ_1 - λ_4 in Figure 4.8 (b)) of the 3D BR. At $\lambda_1=460$ nm, we observed the localized mode of the generation rate at the front portion of the nc-Si:H, which supports the idea that only 3D front contact influences an increase in light absorption on the blue side of the spectrum, since the absorption coefficient of the nc-Si:H is high enough to fully absorb the incident light in the short-wavelength region of the spectrum. (Shah et al., 2004) At λ_2 , λ_3 , and λ_4 , localized modes at the back portion of the nc-Si:H were revealed, resulting from the enhanced scattering and absorption cross sections of the metallic 3D BR and the back-side curvature of the ZnO:Al and nc-Si:H. In addition, high electric field intensities in the nc-Si:H layer were obtained, boosting the absorption of light, and thereby increased photocurrent in the 3D solar cell.

Comparison with thin-film nc-Si:H solar cells employing regular arrays of nanobumps

We compared the 3D solar cell with cells incorporating regular arrays of nanobumps (NBs) via FDTD simulations. Physical dimensions of the cells employing the NB arrays (NBA solar cell hereafter) are based on those of the 3D solar cell (figure 4.11). The diameters of the NBs are taken from the minimum and maximum sizes of the top-view 3D BR, and the height and the periodicity of the NB arrays are same as those of the 3D BR.

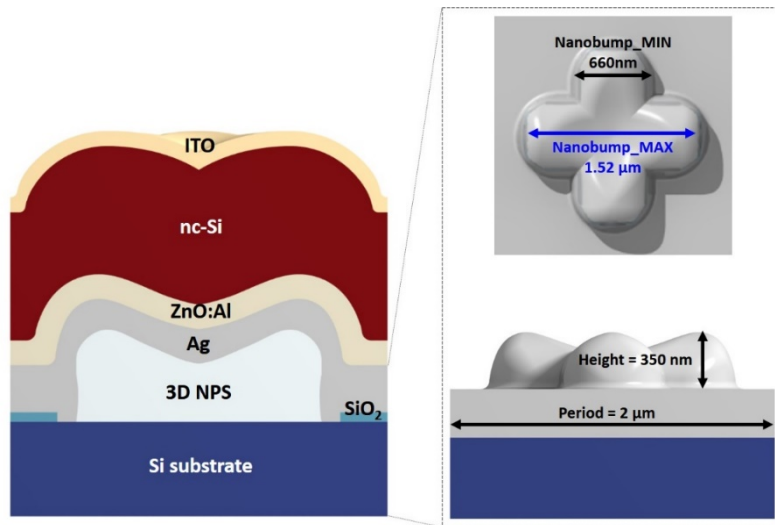


Figure 4.11. Schematic illustration of the cross section of the calculated cell design. The right part of the image shows the detail information of the physical dimensions of the 3D BR.

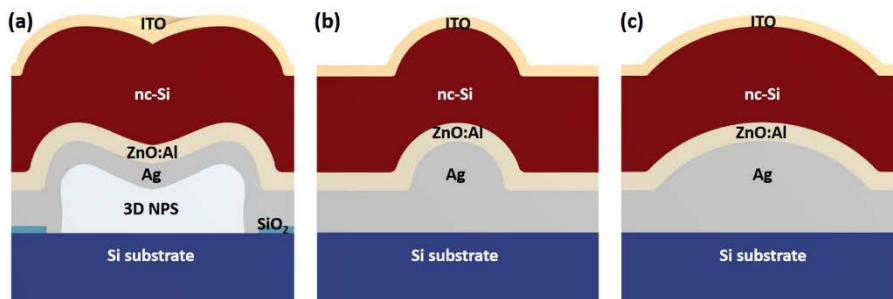


Figure 4.12. Schematic illustration of the cross section of the calculated devices employing diverse nanostructured BRs: (a) 3D BR; regularly ordered nanobumps (NBs) with the (b) minimum (NBA_{min}) and (c) maximum (NBA_{max}) dimensions of the 3D BR as their diameters.

Figure 4.12 exhibits the cross-section views of the simulation models of the 3D, NBA_{min} , and NBA_{max} solar cells. Using these models, absorption curves of the flat, NBA_{min} , NBA_{max} , and 3D solar cells were calculated. As shown in figure 4.13, the 3D solar cell shows the greatest optical performance among the calculated cells. However, the simulated absorption includes the parasitic absorption losses caused by each layer including the Ag, ZnO:Al, and ITO films. Because carriers are generated from a nc-Si:H layer, we isolated the power absorbed in the nc-Si:H as shown in figure 4.14. Through comparing the simulated result of the 3D solar cell with those of the flat, NBA_{min} , and NBA_{max} solar cells, we proved the superior properties of the 3D solar cell. In addition, the carrier generation rates of the 3D, NBA_{min} , and NBA_{max} solar cells were also visualized at $\lambda = 740$ nm representing the resonance wavelength of the 3D BR in figure 4.15. An increase in the electric field intensity in the active material is one of key factors for enhancing absorption of a solar cell. As indicated in figure 4.15, for the case of the 3D solar cell, much enhanced electric field intensities were obtained, and the distributions of localized electric field spread out more than those of the NBA_{min} and NBA_{max} solar cells, which supports the greatest outcomes of the 3D solar cell. Various dimensions and curvatures resulting from the multiscale 3D NPSs induce the high electric field intensity in the nc-Si:H layer, which causes the enhanced carrier generation rates, and thereby the increased photocurrent.

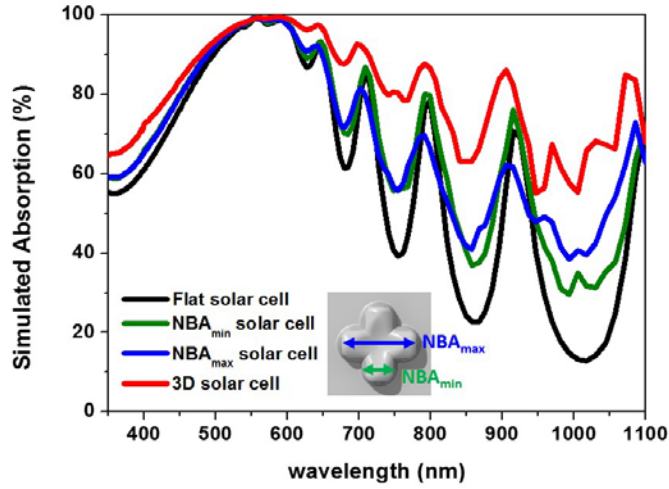


Figure 4.13. Simulated absorption of various thin-film nc-Si:H solar cells. Black and red lines represent the flat and 3D solar cells, respectively. Green and blue lines represent cells employing NBA_{min} and NBA_{max}, respectively.

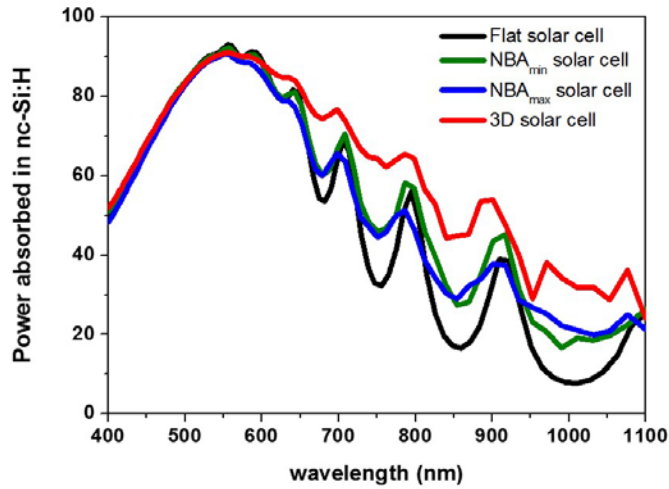


Figure 4.14. Power absorbed in the nc-Si:H layer of the calculated devices. Black and red lines represent the flat and 3D solar cells, respectively. Green and blue lines represent solar cells employing NBA_{min} and NBA_{max}, respectively.

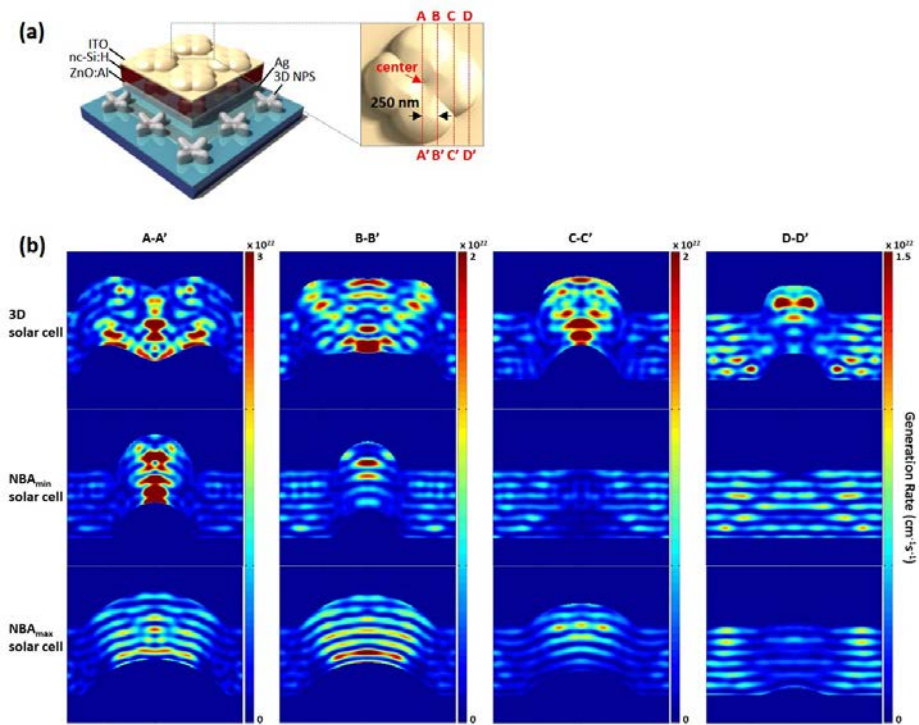


Figure 4.15. (a) Schematic illustration indicating various locations of cross-section views of the 3D solar cell. (b) The cross-section views of the optical generation rates in the nc-Si:H layers of the 3D, NBA_{min}, and NBA_{max} solar cells at the various locations (A-A', B-B', C-C', and D-D').

4.4. Conclusion

we fabricated the thin-film nc-Si:H solar cell on the 3D NPS array with a 20% increase in efficiency compared to the flat cell. At the same time, the 3D solar cell shows optically and electrically improved performance than the cell on the NPCs. Over the entire spectral range where the nc-Si:H is optically active, the 3D-NPS-induced absorption enhancement was observed, leading to 30% enhancement in photocurrent relative to the flat cell. By performing the optical measurements and FDTD analysis, we have revealed that the increased scattering and absorption features by the multiple plasmon resonances and the multiscale roughness of the 3D BR play a key role in enhancing light trapping on the red side of the spectrum. And, it was found that the 3D-textured front contact also causes the localized resonances within the nc-Si:H layer on the blue side of the spectrum. Thus, the combined approach of IAAL and the multi-spark discharge method was demonstrated to break through the technical difficulties in incorporating the complex 3D structures with the efficient light harvesting properties within the inorganic thin-film solar cells, namely the thin-film nc-Si:H solar cell herein. Additionally, the present technique, which can be easily implemented to the various types of solar cells, is expected to open the way for realizing 3D solar cells with high power conversion efficiency.

Chapter 5.

Concluding Remarks

In order to expand the use of the multiscale multidimensional NPSs fabricated by IAAL, we developed the fundamental techniques for the large-area patterning and the sintering of NPSs. Further, we showed the feasibility of the introduced techniques by realizing the 3D solar cell.

In chapter 2, large-scale fabrication of 3D NPSs was carried out via the combination of IAAL and the multi-spark discharge method. The 3D NPSs were constructed over a large area of 50 mm x 50 mm in a parallel manner with ensuring uniformity of above 95%. The morphologies and the porosities of the 3D NPSs were tuned by adjusting the size of nanoparticles generated via the multi-pin SDG. Moreover, various 3D NPSs were produced by controlling the pattern shape of the insulating layers and the deposition time. We also demonstrated the 3D light back reflectors showing much more enhanced diffuse reflectivity compared to the 1D and 2D light back reflectors.

In chapter 3, we proposed a new methodology for improving stiffness of NPSs via e-beam irradiation. The physical properties of the NPSs were adjusted with respect to the e-beam irradiation conditions. The combined method of IAAL and the e-beam sintering method created NPSs with the novel morphologies by restructuring the NPSs via IAAL.

In the last chapter, we fabricated the thin-film nc-Si:H solar cell incorporating the 3D NPS array based on the two techniques in chapter 2 and 3, which showed optically and electrically the greatest performance than the flat and NPC solar cells. The improvement in efficiency is mainly attributed to the enhanced photocurrent resulting from the increased light

trapping effect induced by the 3D NPSs. For further understanding of the greatest outcome of the 3D solar cell, electromagnetic modeling by FDTD simulations was carried out to investigate the roles of the 3D BR and the 3D front contact as well as carrier generation rates in the nc-Si:H layers in the 3D solar cell.

Acknowledgement

This work was supported by the Global Frontier R&D Program on Center for Multiscale Energy System funded by the National Research Foundation under the Ministry of Education, Science and Technology, Korea (2011-0031561 and 2012M3A6A7054855). Most of all, I would like to thank my advisor professor Mansoo Choi. And I would like to thank professor Jong-Kwon Lee, doctor Jun-Sik Cho, and doctor Min Seok Jang for their help and thoughtful consideration. All of my laboratory members helped me with great passion. Especially, I want to thank Hoseop Choi, Segeun Jang, and Taemin Lee for their help in my researches.

References

- R. Lakes, Materials with structural hierarchy, *Nature*, 361, 511, 1993.
- H. C. Ko, M. P. Stoykovich, J. Song, V. Malyarchuk, W. M. Choi, C.-J. Yu, J. B. Geddes, J. Xiao, S. Wang, Y. Huang, and J. A. Rogers, A hemispherical electronic eye camera based on compressible silicon optoelectronics, *Nature*, 454, 748, 2008.
- E. C. Yusko, J. M. Johnson, S. Majd, P. Prangkio, R. C. Rollings, J. Li, J. Yang, and M. Mayer, Controlling protein translocation through nanopores with bio-inspired fluid walls, *Nat. Nanotechnol.*, 6, 253, 2011.
- C. Ye, L. Zhang, X. Fang, Y. Wang, P. Yan, and J. Zhao, Hierarchical structure: Silicon nanowires standing on silica microwires, *Adv. Mater.*, 16, 1019, 2004.
- Y. T. Tseng, W. H. Tseng, C. H. Lin, and R. M. Ho, Fabrication of double-length-scale patterns via lithography, block copolymer templating, and electrodeposition, *Adv. Mater.*, 19, 3584, 2007.
- J. Henzie, M. H. Lee, and T. W. Odom, Multiscale patterning of plasmonic metamaterials, *Nat. Nanotechnol.*, 2, 549, 2007.
- G. A. Wurtz, R. Pollard, W. Hendren, G. P. Wiederrecht, D. J. Gosztola, V. A. Podolskiy, and A. V. Zayats, Designed ultrafast optical nonlinearity in a

- plasmonic nanorod metamaterial enhanced by nonlocality, *Nat. Nanotechnol.*, 6, 107, 2011.
- R. Srivastava, M. Choi, and R. Ryoo, Mesoporous materials with zeolite framework: remarkable effect of the hierarchical structure for retardation of catalyst deactivation, *Chem. Commun.*, 43, 4489, 2006.
- M. Choi, K. Na, J. Kim, Y. Sakamoto, O. Terasaki, and R. Ryoo, Stable single-unit-cell nanosheets of zeolite MFI as active and long-lived catalysts, *Nature*, 461, 246, 2009.
- Z. Nie and E. Kumacheva, Patterning surfaces with functional polymers, *Nat. Mater.*, 7, 277, 2008.
- A. Carlson, A. M. Bowen, Y. Huang, R. G. Nuzzo, and J. A. Rogers, Transfer printing techniques for materials assembly, and micro/nanodevice Fabrication, *Adv. Mater.* 24, 5284, 2012.
- W. Bae, H. Kim, D. Kim, S. Park, H. Jeong, and K. Shu, 25th anniversary article: scalable multiscale patterned structures inspired by nature: the role of hierarchy, *Adv. Mater.*, 26, 675, 2014.
- J. H. Cho and D. H. Gracias, Self-assembly of lithographically patterned nanoparticles, *Nano Letters*, 9, 4049, 2009.

- H. Fudouzi, M. Kobayashi, and N. Shinya, Site-controlled deposition of microsized particles using an electrostatic assembly, *Adv. Mater.*, 14, 1649, 2002.
- S. F. Lyuksyutov, R. A. Vaia, P. B. Paramonov, S. Juhl, L. Waterhouse, R. M. Ralich, G. Sigalov, and E. Sancaktar, Electrostatic nanolithography in polymers using atomic force microscopy, *Nat. Mater.*, 2, 468, 2003.
- D. Xia, Z. Ku, S. C. Lee, and S. R. J. Brueck, Nanostructures and functional materials fabricated by interferometric lithography, *Adv. Mater.*, 23, 147, 2011.
- C. A. Ross, K. K. Berggren, J. Y. Cheng, Y. S. Jung, and J.-B. Chang, Three-dimensional nanofabrication by block copolymer self-assembly, *Adv. Mater.*, 26, 4386, 2014.
- H. Kim, J. Kim, H. Yang, J. Suh, T. Kim, B. Han, S. Kim, D. S. Kim, P. V. Pikhitsa and M. Choi, Parallel patterning of nanoparticles via electrodynamic focusing of charged aerosols, *Nat. Nanotechnol.*, 1, 117-121, 2006.
- H. Lee, S. You, C. G. Woo, K. Lim, K. Jun and M. Choi, Focused patterning of nanoparticles by controlling electric field induced particle motion, *Appl. Phys. Lett.*, 94, 053104 (3pp), 2009.

- H. Lee, S. You, P. V. Pikhitsa, J. Kim, S. Kwon, C. G. Woo, and M. Choi, Three-dimensional assembly of nanoparticles from charged aerosols, *Nano Lett.*, 11, 119-124, 2010.
- S. You, K. Han, H. Kim, H. Lee, C. G. Woo, C. Jeong, W. Nam and M. Choi, High-resolution, parallel patterning of nanoparticles via an ion-induced focusing mask, *Small*, 6, 2146-2152, 2010.
- C. G. Woo, H. Shin, C. Jeong, K. Jun, J. Lee, J. Lee, H. Lee, S. You, Y. Son and M. Choi, Selective nanopatterning of protein via ion-induced focusing and its application to metalenhanced fluorescence, *Small*, 7, 1790-1794, 2011.
- D. Kim, P. V. Pikhitsa, H. Yang and M. Choi, Room temperature CO and H₂ sensing with carbon nanoparticles, *Nanotechnology*, 22, 485501 (7pp), 2011.
- K. Jung, J. Hahn, S. In, Y. Bae, H. Lee, P. V. Pikhitsa, K. Ahn, K. Ha, J. Lee, N. Park, and M. Choi, Hotspot-engineered 3D multipetal flower assemblies for surface-enhanced Raman spectroscopy, *Adv. Mater.*, 26, 5924-5929, 2014.
- K. Ha, H. Choi, K. Jung, K. Han, J. Lee, K. Ahn and M. Choi, Large-area assembly of three-dimensional NPSs via ion assisted aerosol lithography with a multi-pin spark discharge generator, *Nanotechnology*, 25, 225302 (9pp), 2014.

- K. Han, W. Kim, J. Yu, J. Lee, H. Lee, C. G. Woo, and M. Choi, A study of pin-to-plate type spark discharge generator for producing unagglomerated nanoaerosols, *J. Aerosol Sci.*, 52, 80-88, 2012.
- A. Dong, J. Chen, S. J. Oh, W.-K. Koh, F. Xiu, X. Ye, D.-K. Ko, K. L. Wang, C. R. Kagan and C. B. Murray, Multiscale periodic assembly of striped nanocrystal superlattice films on a liquid surface, *Nano Lett.*, 11, 841, 2011.
- K. G. A. Tavakkoli, K. W. Gotrik, A. F. Hannon, A. Alexander-Katz, C. A. Ross and K. K. Berggren, Templating three-dimensional self-assembled structures in bilayer block copolymer films, *Science*, 336, 1294, 2012.
- G. Liu, A. Ramírez-Hernández, H. Yoshida, K. Nygård, D. K. Satapathy, O. Bunk, J. J. de Pablo and P. F. Nealey, Morphology of lamellae-forming block copolymer films between two orthogonal chemically nanopatterned striped surfaces, *Phys. Rev. Lett.*, 108, 065502, 2012.
- C. A. Mirkin, R. L. Letsinger, R. C. Mucic and J. J. Storhoff, A DNA-based method for rationally assembling nanoparticles into macroscopic materials, *Nature*, 382, 607, 1996.
- C. Chi, F. Vargas-Lara, A. V. Tkachenko, F. W. Starr and O. Gang, Internal structure of nanoparticle dimers linked by DNA, *ACS Nano*, 6, 6793, 2012.

- J. Mu, C. Shao, Z. Guo, M. Zhang, Z. Zhang, P. Zhang, B. Chen and Y. Liu, Solvothermal synthesis and electrochemical properties of 3D flower-like iron phthalocyanine hierarchical nanostructure, *Nanoscale*, 3, 5126, 2011.
- Z. Bian, J. Zhu, J. Wang, S. Xiao, C. Nuckolls and H. Li, Multitemplates for the hierarchical synthesis of diverse inorganic materials, *J. Am. Chem. Soc.*, 134, 2325, 2012.
- O. S. Kwon, S. J. Park, J. S. Lee, E. Park, T. Kim, H. W. Park, S. A. You, H. Yoon and J. Jang, Multidimensional conducting polymer nanotubes for ultrasensitive chemical nerve agent sensing, *Nano Lett.*, 12, 2797, 2012.
- Y. J. Hwang, C. H. Wu, C. Hahn, H. E. Jeong and P. Yang, Si/InGaN core/shell hierarchical nanowire arrays and their photoelectrochemical properties, *Nano Lett.*, 12, 1678, 2012.
- J. Kim, Y. Piao and T. Hyeon, Multifunctional nanostructured materials for multimodal imaging, and simultaneous imaging and therapy, *Chem. Soc. Rev.*, 38, 372, 2009.
- J. Gao, H. Gu and B. Xu, Multifunctional magnetic nanoparticles: design, synthesis, and biomedical applications, *Acc. Chem. Res.*, 42, 1097, 2009.
- G. Freymann, A. Ledermann, M. Thiel, I. Staude, S. Essig, K. Busch and M. Wegener, Three-dimensional nanostructures for photonics, *Adv. Func. Mater.*, 20, 1038, 2010.

- Y. Zhang, N. K. Grady, C. Ayala-Orozco and N. J. Halas, Three-dimensional nanostructures as highly efficient generators of second harmonic light, *Nano Lett.*, 11, 5519, 2011.
- T. Ergin, N. Stenger, P. Brenner, J. B. Pendry and M. Wegener, Three-dimensional invisibility cloak at optical wavelengths, *Science*, 328, 337, 2010.
- A. Ponzoni, E. Comini, G. Sberveglieri, J. Zhou, S. Z. Deng, N. S. Xu, Y. Ding and Z. L. Wang, Ultrasensitive and highly selective gas sensors using three-dimensional tungsten oxide nanowire networks, *Appl. Phys. Lett.*, 88, 203101, 2006.
- V. Polshettiwar, B. Baruwati and R. S. Varma, Self assembly of metal oxides into three-dimensional nanostructures: synthesis and application in catalysis, *ACS Nano*, 3, 728, 2009.
- G. Tian, Y. Chen, W. Zhou, K. Pan, C. Tian, X.-r. Huang and H. Fu, 3D hierarchical flower-like TiO₂ nanostructure: morphology control and its photocatalytic property, *CrystEngComm.*, 13, 2994, 2011.
- B. O. Mueller, M. E. Messing, D. L. J. Engberg, A. M. Jansson, L. I. M. Johansson, S. M. Norlén, N. Tureson and K. Deppert, Review of spark discharge generators for production of nanoparticle aerosols, *Aerosol Sci. Technol.*, 46, 1256, 2012.

- N. S. Tabrizi, M. Ullmann, V. A. Vons, U. Lafont and A. Schmidt-Ott, Generation of nanoparticles by spark discharge, *J. Nanopart. Res.*, 11, 315, 2009.
- S. Schwyn, E. Garwin and A. Schmidt-Ott, Aerosol generation by spark discharge, *J. Aerosol Sci.*, 19, 639, 1988.
- M. T. Swihart, Vapor-phase synthesis of nanoparticles, *Curr. Opin. Colloid. Interface Sci.*, 8, 127, 2003.
- F. E. Kruis, H. Fissan and A. Peled, Synthesis of nanoparticles in the gas phase for electronic, optical and magnetic applications—a review, *J. Aerosol Sci.*, 29, 511, 1998.
- N. S. Tabrizi, Q. Xu, N. M. van der Pers, U. Lafont and A. Schmidt-Ott, Synthesis of mixed metallic nanoparticles by spark discharge, *J. Nanopart. Res.*, 11, 1209, 2009.
- J. H. Byeon, J. H. Park and J. Hwang, Spark generation of monometallic and bimetallic aerosol nanoparticles, *J. Aerosol Sci.*, 39, 888, 2008.
- Y. Min, M. Akbulut, K. Kristiansen, Y. Golan and J. Israelachvili, The role of interparticle and external forces in nanoparticle assembly, *Nat. Mater.*, 7, 527, 2008.

- H. Fudouzi, M. Kobayashi and N. Shinya, Site-controlled deposition of microsized particles using an electrostatic assembly, *Adv. Mater.*, 14, 1649, 2002.
- T. J. Krinke, H. Fissan, K. Deppert, M. H. Magnusson and L. Samuelson, Positioning of nanometer-sized particles on flat surfaces by direct deposition from the gas phase, *Appl. Phys. Lett.*, 78, 3708, 2001.
- T. J. Krinke, K. Deppert, M. H. Magnusson and H. Fissan, Nanostructured deposition of nanoparticles from the gas phase, *Part. Part. Syst. Char.*, 19, 321, 2002.
- W. Prost, F. E. Kruis, F. Otten, K. Nielsch, B. Rellinghaus, U. Auer, A. Peled, E. F. Wassermann, H. Fissan and F. J. Tegude, Monodisperse aerosol particle deposition: prospects for nanoelectronics, *Microelectron. Eng.*, 41–42, 535, 1998.
- S. A. Maier. 2007, *Plasmonics: Fundamentals and Applications* (New York: Springer)
- J. A. Rogers, M. Meier, A. Dodabalapur, E. J. Laskowski, and M. A. Cappuzzo, Distributed feedback ridge waveguide lasers fabricated by nanoscale printing and molding on nonplanar substrates, *Appl. Phys. Lett.*, 74, 3257, 1999.
- Z. Nie, and E. Kumacheva, Patterning surfaces with functional polymers, *Nat. Mater.*, 7, 277, 2008.

- A. Carlson, A. M. Bowen, Y. Huang, R. G. Nuzzo, and J. A. Rogers, Transfer Printing techniques for materials assembly and micro/nanodevice fabrication, *Adv. Mater.* 24, 5284, 2012.
- W.-G. Bae, H. N. Kim, D. Kim, S.-H. Park, H. E. Jeong, and K.-Y. Suh, 25th anniversary article: scalable multiscale patterned structures inspired by nature: the role of hierarchy, *Adv. Mater.*, 26, 675, 2014.
- Y. Xia and G. M. Whitesides, Soft lithography, *Annu. Rev. Mater. Sci.* 28, 153, 1998.
- L. J. Guo, Nanoimprint lithography: methods and material requirements, *Adv. Mater.*, 19, 495, 2007.
- B. D. Gates, Nanofabrication with molds & stamps, *Mater. Today*, 8, 44, 2005.
- K. Y. Suh, M. C. Park, and P. Kim, Capillary force lithography: A versatile tool for structured biomaterials interface towards cell and tissue engineering, *Adv. Funct. Mater.*, 19, 2699, 2009.
- M. A. Meitl, Z.-T. Zhu, V. Kumar, K. J. Lee, X. Feng, Y. Y. Huang, I. Adesida, R. G. Nuzzo, and J. A. Rogers, Transfer printing by kinetic control of adhesion to an elastomeric stamp, *Nat. Mater.* 5, 33, 2005.
- G. M. Whitesides and B. Grzybowski, Self-assembly at all scales, *Science*, 295, 2418, 2002.

- M. Matsusaki, H. Ajiro, T. Kida, T. Serizawa, and M. Akashi, Layer-by-layer assembly through weak interactions and their biomedical applications, *Adv. Mater.*, 24, 454, 2012.
- Y. Xie, Y. Qian, W. Wang, S. Zhang, and Y. Zhang, A benzene-thermal synthetic route to nanocrystalline GaN, *Science*, 272, 1926, 1996.
- J. Y. Cheng, C. A. Ross, H. I. Smith, and E. L. Thomas, Templated self-assembly of block copolymers: top-down helps bottom-up, *Adv. Mater.* 18, 2505, 2006.
- Y. Rahmawan, M. W. Moon, K. S. Kim, K. R. Lee, and K. Y. Suh, Wrinkled, dual-scale structures of diamond-like carbon (DLC) for superhydrophobicity, *Langmuir*, 26, 484, 2010.
- W.-Y. Yeong, C.-K. Chua, K.-F. Leong, and M. Chandrasekaran, Rapid prototyping in tissue engineering: challenges and potential, *Trends Biotechnol.* 22, 643, 2004.
- T. T. Tsong, Effects of an electric field in atomic manipulations, *Phys. Rev. B: Condens. Matter Mater. Phys.*, 44,13703, 1991.
- R. J. Barsotti, M. D. Vahey, R. Wartena, Y.-M. Chiang, J. Voldman, and F. Stellacci, Assembly of metal nanoparticles into nanogaps, *Small* 3, 488, 2007.

- L. Bernard, M. Calame, S. J. v. d. Molen, J. Liao, and C. Schönenberger, Controlled formation of metallic nanowires via Au nanoparticle AC Trapping, *Nanotechnology*, 18, 235202, 2007.
- C. Yilmaz A. E. Cetin, G. Goutzamanidis, J. Huang, S. Somu, H. Altug, D. Wei, and A. Busnaina, Three-dimensional crystalline and homogeneous metallic nanostructures using directed assembly of nanoparticles, *ACS Nano*, 8, 4547, 2014.
- D. Maugis and H. M. Pollock, Surface forces, deformation and adherence at metal microcontacts, *Acta Metall.* 32, 1323, 1984.
- U. Ramsperger, T. Uchihashi, and H. Nejh, Fabrication and lateral electronic transport measurements of gold nanowires, *Appl. Phys. Lett.*, 78, 85, 2001.
- M. Calleja, M. Tello Ruiz, J. V. Anguita, F. Garca, and R. Garca Garca, Fabrication of gold nanowires on insulating substrates by field-induced mass transport, *Appl. Phys. Lett.*, 79, 2471, 2001.
- Z. Zou, J. Kai, and C. H. Ahn, Electrical characterization of suspended gold nanowire bridges with functionalized self-assembled monolayers using a top-down fabrication method, *J. Micromech. Microeng.* 19, 055002, 2009.
- C. Durkan and M. E. Welland, Size effects in the electrical resistivity of polycrystalline nanowires. *Phys. Rev. B: Condens. Matter Mater. Phys.* 61, 14215, 2000.

- S. H. Ko, I. Park, H. Pan, C. P. Grigoropoulos, A. P. Pisano, C. K. Luscombe, and J. M. Frechet, Direct nanoimprinting of metal nanoparticles for nanoscale electronics fabrication, *Nano Lett.* 7, 1869, 2007.
- S. Guldin, Sven Hu'ttner, M. Kolle, M. E. Welland, P. M. Buschbaum, R. H. Friend, U. Steiner, and N. Te'treault, Dye-sensitized solar cell based on a three-dimensional photonic crystal, *Nano Lett.*, 10, 2303-2309, 2010.
- S. H. Ko, D. Lee, H. W. Kang, K. H. Nam, J. Y. Yeo, S. J. Hong, C. P. Grigoropoulos, and H. J. Sung, Nanoforest of hydrothermally grown hierarchical ZnO nanowires for a high efficiency dye-sensitized solar cell, *Nano Lett.*, 11, 666-671, 2011.
- H. K. Yu, W. J. Dong, G. H. Jung, and J.-L. Lee, Three-dimensional nanobranched indium-tin-oxide anode for organic solar cells, *ACS Nano*, 5, 8026-8032, 2011.
- H. Kwon, J. Ham, D. Y. Kim, S. J. Oh, S. Lee, S. H. Oh, E. F. Schubert, K.-G. Lim, T.-W. Lee, S. Kim, J.-L. Lee, and J. K. Kim, Three-dimensional nanostructured indium-tin-oxide electrodes for enhanced performance of bulk heterojunction organic solar cells, *Adv. Energy Mater.*, 4, 1301566 (7pp), 2014.
- H. A. Atwater and A. Polman, Plasmonics for improved photovoltaic devices, *Nat. Mater.*, 9, 205-213, 2010.

- S.-W. Baek, G. Park, J. Noh, C. Cho, C.-H. Lee, M.-K. Seo, H. Song, and J.-Y. Lee, Au@Ag core-shell nanocube for efficient plasmonic light trapping effect in low bandgap organic solar cells, *ACS Nano*, 8, 3302-3312, 2014.
- S.-C. Chen, Y.-J. Chen, W. T. Chen, Y.-T. Yen, T. S. Kao, T.-Y. Chuang, Y.-K. Liao, K.-H. Wu, A. Yabushita, T.-P. Hsieh, M. D. B. Charlton, D. P. Tsai, H.-C. Kuo, and Y.-L. Chueh, Toward omnidirectional light absorption by plasmonic effect for high-efficiency flexible nonvacuum Cu(In,Ga)Se₂ thin film solar cells, *ACS Nano*, 8, 9341-9348, 2014.
- E. Garnett and P. Yang, Light trapping in silicon nanowire solar cells, *Nano Lett.*, 10, 1082-1087, 2010.
- X. Liu, B. Wu, Q. Zhang, J. N. Yip, G. Yu, Q. Xiong, N. Mathews, and T. C. Sum, Elucidating the localized plasmonic enhancement effects from a single Ag nanowire in organic solar cells, *ACS Nano*, 8, 10101-10110, 2014.
- L. M.-Meskamp, Y. H. Kim, T. Roch, S. Hofmann, R. Scholz, S. Eckardt, K. Leo and A. F. Lasagni, Efficiency enhancement of organic solar cells by fabricating periodic surface textures using direct laser interference patterning, *Adv. Mater.*, 24, 906-910, 2012.
- V. E. Ferry, J. N. Munday and H. A. Atwater, Design considerations for plasmonic photovoltaics, *Adv. Mater.*, 22, 4794-4808, 2010.

- J. Zhu, C.-M. Hsu, Z. Yu, S. Fan and Y. Cui, Nanodome solar cells with efficient light management and self-cleaning, *Nano Lett.*, 10, 1979-1984, 2010.
- V. E. Ferry, A. Polman, and H. A. Atwater, Modeling light trapping in nanostructured solar cells, *ACS Nano*, 5, 10055-10064, 2011.
- M. G. Deceglie, V. E. Ferry, A. P. Alivisatos, and H. A. Atwater, Design of nanostructured solar cells using coupled optical and electrical modeling, *Nano Lett.*, 12, 2894-2900, 2012.
- C.-M. Hsu, C. Battaglia, C. Pahud, Z. Ruan, F.-J. Haug, S. Fan, C. Ballif and Y. Cui, High-efficiency amorphous silicon solar cell on a periodic nanocone back reflector, *Adv. Energy Mater.*, 2, 628-633, 2012.
- A. Mihi, F. J. Beck, T. Lasanta, A. K. Rath and G. Konstantatos, Imprinted electrodes for enhanced light trapping in solution processed solar cells, *Adv. Mater.*, 26, 443-448, 2014.
- H. B.T. Li, R. H. Franken, J. K. Rath, R. E.I. Schropp, Structural defects caused by a rough substrate and their influence on the performance of hydrogenated nano-crystalline silicon n-i-p solar cells, *Sol. Energy Mater. Sol. Cells*, 93, 338-349, 2009.
- M. Python, O. Madani, D. Dominé, F. Meillaud, E. Vallat-Sauvain, C. Ballif, Influence of the substrate geometrical parameters on microcrystalline

- silicon growth for thin-film solar cells, *Sol. Energy Mater. Sol. Cells*, 93, 1714-1720, 2009.
- S. A. Maier and H. A. Atwater, Plasmonics: Localization and guiding of electromagnetic energy in metal/dielectric structures, *J. Appl. Phys.*, 98, 011101 (10pp), 2005.
- T. R. Jensen, M. L. Duval, K. L. Kelly, A. A. Lazarides, G. C. Schatz and R. P. Van Duyne, Nanosphere lithography: Effect of the external dielectric medium on the surface plasmon resonance spectrum of a periodic array of silver nanoparticles, *J. Phys. Chem. B*, 103, 9846-9853, 1999.
- E. D. Palik, Handbook of optical constants of solids III, Academic, New York, 1998.
- A. D. Yaghjian, Internal energy, Q-Energy, Poynting's theorem, and the stress dyadic in dispersive material, *IEEE Trans. Antennas Propag.*, 55, 1495-1505, 2007.
- A. V. Shah, H. Schade, M. Vanecek, J. Meier, E. Vallat-Sauvain, N. Wyrsh, U. Kroll, C. Droz and J. Bailat, Thin-film silicon solar cell technology, *Prog. Photovolt: Res. Appl.*, 12, 113-142, 2004.

국문 초록

멀티스케일 다차원 나노입자 구조물 대면적 조립 및 재구조화 이의 태양전지 응용

서울대학교 대학원 기계항공공학부

하 경 연

최근 나노스케일 물질의 독특하고 우수한 특성을 과학 및 공학의 여러 분야에 적용하고자, 나노 물질 개발 연구가 전 세계적으로 진행되고 있다. 그 중에서도, 나노스케일을 넘어, 멀티스케일 다차원 구조물의 복합적인 특성을 여러 응용분야에 활용하기 위해, 나노구조물 형성 기술에 대한 관심이 지속적으로 높아지고 있다. 한 노력으로, 본 연구실에서는 전기장 내 입자 거동 제어를 이용한 다차원 나노입자 어셈블리 기술을 개발하였으며, 본 기술로 형성된 3차원 구조물의 우수한 특성을 보임으로써 기술의 우수성을 증명하였으나, 기술의 적용가능성을 넓히기 위해서는 대면적 패터닝 연구와 구조물의 강성 증가 연구가 필수이다. 이러한 동기로, 본 연구에서는, 나노입자 어셈블리 기술을 통해 형성된 멀티스케일 다차원 구조물의 적용가능성을 넓히는 기반 기술을 개발하고, 그 기반

기술의 응용가능성을 증명하는 것을 목표로 하였다.

먼저, 새롭게 제안한 멀티스파크 방전법과 다차원 나노입자 어셈블리 기술을 접목한 멀티스케일 다차원 나노입자 구조물의 대면적 패터닝 기술을 개발하였고, 3차원 나노입자 구조물을 50 mm x 50 mm의 대면적에 균일하게 형성하는 것을 성공적으로 수행하였다. 이 과정 중, 나노입자 크기 제어를 이용한 3차원 나노입자 구조물 형상 변화 연구를 수행함으로써 대면적 패터닝 기술의 활용가능성을 확인하였다. 뿐만 아니라, 기존 반도체 공정기술로 형성한 후면 반사체보다 우수한 특성을 지닌 3차원 후면 반사체를 구현함으로써, 대면적 패터닝 기술의 응용가능성 또한 확증하였다.

멀티스케일 다차원 구조물의 적용가능성을 넓히기 위한 또다른 연구로, 나노입자 구조물의 강성을 증가시키는 연구를 수행하였다. 전자빔을 이용한 소결법으로, 소결되는 원리 파악 및 소결과정 중 나노입자 구조물의 물리적 특성 변화를 실험적으로 관찰하였다. 또한, 전자빔 소결 기술과 나노입자 어셈블리 기술을 접목하여 일차적으로 형성된 3차원 나노입자 구조물을 재구조화하는 연구를 수행하여, 기존 기술로 구현하기 어려운 독창적인 나노구조물을 형성함으로써, 나노입자 어셈블리 기술을 응용 및 확장하였다.

앞서 수행한 두 연구와 나노입자 어셈블리 기술의 적용가능성을 보이기 위해, 3차원 나노입자 구조물을 이용한 박막 실리콘 태양전지를 제작하였다. 3차원 나노입자 구조물을 통한 빛 가둠 현상 극대화를 목표로 한 연구로, 나노입자

클러스터와의 실험적 비교 및 나노범프 어레이와의 이론적 비교를 통해 3차원 나노입자 구조물의 우수한 광학적 특성을 확인하였다. 또한, 실제 박막 실리콘 태양전지에 각 구조물을 적용하고, 이를 비교평가하여 3차원 나노입자 구조물을 적용한 박막 실리콘 태양전지가 가장 우수한 특성을 보이는 것과 평평한 태양전지 대비 단락 전류밀도 30%, 효율 20%가 증가하는 것을 확인하였다.

주요어: 나노입자; 어셈블리; 스파크 방전; 대면적 형성; 전자빔; 소결; 태양전지; 빛 가둠; 3차원 구조물
학 번: 2009-20737